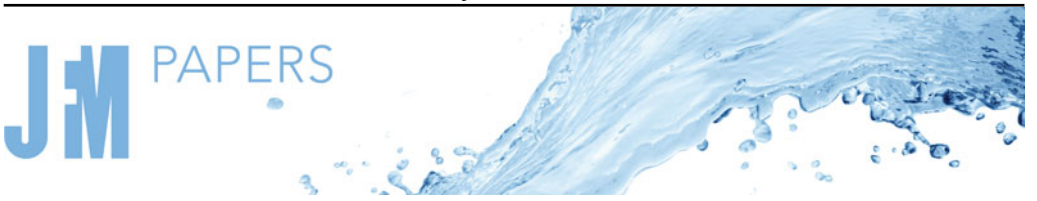
J. Fluid Mech. (2026), *vol.* 1031, A11, doi:10.1017/jfm.2026.11255



Resolvent analysis of shock-laden flows

Sandeep Ravikumar Murthy[1] and **Daniel J. Bodony**[1]

[1]Department of Aerospace Engineering, University of Illinois at Urbana-Champaign, Urbana, USA

Corresponding author: Sandeep Ravikumar Murthy, sandeep.murthy1@gmail.com

(Received 10 April 2025; revised 25 November 2025; accepted 18 January 2026)

We present a semi-analytic investigation of the resolvent operator, and its associated forcing and response modes for quasi-one-dimensional shock-laden flows. Using a Green's function approach, we derive resolvent solutions for isentropic (subsonic and supersonic) and transonic flows with shocks in converging–diverging nozzles of arbitrary geometry. Our analysis demonstrates that shock-induced heightened sensitivity in the resolvent across flow discontinuities leads to significant discrepancies between numerically computed and the analytical input and output modes if shock effects are not properly accounted for. In particular, we find that the resolvent operator exhibits singular behaviour at the shock location. Specifically, the inviscid (where the shock is treated purely as a flow discontinuity) and viscous analytical leading resolvent modes do not converge as the viscosity parameter $\mu \to 0$, which affects the accuracy of flow control and stability analyses that rely on resolvent-based methods. Furthermore, the derived solutions serve as benchmarks for verifying numerical schemes designed to compute adjoint and resolvent modes in shock-laden flows, ensuring that they capture the correct physical behaviour in the presence of shocks.

Key words: shock waves, computational methods

1. Introduction

Resolvent analysis has emerged as a powerful tool in fluid mechanics for understanding and predicting the response of fluid flows to external forcings (Schmid 2007; McKeon & Sharma 2010). By identifying the forcing-response pairs of a dynamical system under harmonic excitation, resolvent analysis aids in uncovering the mechanisms underlying flow instabilities and interpreting turbulent dynamics. These insights are instrumental in various applications, including for example, flow control strategies, noise reduction and the design of more efficient aerodynamic systems.

© The Author(s), 2026. Published by Cambridge University Press. This is an Open Access article, distributed under the terms of the Creative Commons Attribution licence (https://creativecommons.org/licenses/by/4.0/), which permits unrestricted re-use, distribution and reproduction, provided the original article is properly cited.

https://doi.org/10.1017/jfm.2026.11255 Published online by Cambridge University Press

The forcing and response mode pairs obtained from resolvent analysis also provide valuable information about the structural sensitivity of a flow to localised feedback mechanisms (Qadri & Schmid 2017). This sensitivity analysis can be used to identify regions within the flow where small perturbations can lead to significant changes, thereby informing the optimal placement of sensors and actuators for flow control applications. Examples include controlling cavity flows (Qadri & Schmid 2017) and reducing jet noise (Murthy & Bodony 2024).

Despite the extensive application of resolvent analysis to various flow configurations, and the development of effective numerical techniques, including matrix-free iterative techniques (Bagheri, Brandt & Henningson 2009; Monokrousos, Brandt & Henningson 2010; Loiseau *et al.* 2019; Martini *et al.* 2020), randomised numerical linear algebra methods (Liberty *et al.* 2007; Halko, Martinsson & Tropp 2011; Moarref *et al.* 2013) and a recent purely data-driven approach detailed by Herrmann *et al.* (2021), the extension of resolvent analysis to shock-laden flows remains insufficiently explored. Shock waves introduce discontinuities in the flow properties, leading to complexities in the linearised operators and sensitivities that are not present in smooth flows. The presence of shocks poses significant challenges in both the theoretical understanding and numerical computation of resolvent modes. Notably, there is a lack of analytical solutions against which numerically computed resolvents in shock-laden flows can be verified.

It has long been recognised that an inviscid linearisation of a shock wave is ill-posed unless the Rankine–Hugoniot jump conditions are imposed as an internal boundary: without them, the spectrum becomes pathological, admitting continuous branches and unbounded growth (Guderley 1942; D'yakov 1954). Viscous regularisation remedies this behaviour and restores a discrete, well-posed operator, as established in classical shock-stability studies (Mack 1984; Fedorov 2011). The present work builds upon their contributions by supplying the first semi-analytic resolvent benchmark that embeds the Rankine–Hugoniot conditions and viscous effects, enabling quantitative verification of fully numerical resolvent solvers in shock-laden flows.

Additionally, prior studies have addressed related issues in the context of adjoint solutions in inviscid flows with shocks. In addition to their relevance for adjoint-based analyses, shock waves play a crucial role in transonic aerodynamic optimisation, which has become a topic of growing interest. Adjoint methods have proven particularly effective for managing shocks, as they enable the efficient computation of sensitivity gradients for performance metrics with respect to design changes (Li *et al.* 2024). Furthermore, aerodynamic shape optimisation remains a central strategy in shock management. Studies have shown that refining wing configurations in supersonic aircraft, through adjustments to parameters such as leading-edge sweep angles and aspect ratios, effectively delays shock wave onset and mitigates drag penalties (Reuther *et al.* 1999). Giles *et al.* (1997) and Giles & Pierce (2000, 2001) examined the properties of adjoint solutions in such flows, highlighting the need for careful treatment of discontinuities. More recently, Bodony & Fikl (2022) investigated the numerical implications of adjoint methods in the presence of shocks, emphasising the importance of using appropriate numerical schemes to achieve convergence. Collectively, these developments underscore the critical importance of addressing shock phenomena in aerodynamic optimisation, paving the way for the design of highly efficient and high-performance aerodynamic systems.

Motivated by these challenges, the present study aims to investigate the impact of flow discontinuities on the forcing-response dynamics of simple shock-laden flows. Specifically, we focus on developing semi-analytic resolvent solutions for the quasi-one-dimensional Euler and Navier–Stokes equations governing flow in a converging–diverging nozzle of arbitrary shape. By using a Green's function approach, we construct both

https://doi.org/10.1017/jfm.2026.11255 Published online by Cambridge University Press

inviscid and viscous Green's function operators corresponding to the forward and adjoint operators. These operators incorporate extensions that allow shocks to be included explicitly in the problem formulation.

The objectives of this study are threefold.

(i) Derive semi-analytic resolvent solutions for isentropic (subsonic and supersonic) and transonic flows with shocks, providing a benchmark for verifying numerical resolvent analyses in shock-laden flows.
(ii) Analyse the sensitivity of the resolvent solutions to disturbances across flow discontinuities, elucidating the impact of shocks on the forcing-response dynamics.
(iii) Assess the validity of numerical schemes used for computing adjoint and resolvent solutions in the presence of shocks, particularly those recommended by Bodony & Fikl (2022).

Our presentation is structured as follows. We begin with an introduction to resolvent analysis in § 2, and then introduce the inviscid problem in § 3, deriving the forward and adjoint Green's function operators, and constructing the zero-frequency resolvent operator. Next, we extend the analysis to viscous shock-laden flows in § 4, highlighting the role of viscosity in resolving discrepancies between numerical and semi-analytic resolvent solutions. In § 5, we introduce a modified WENO formulation tailored for resolvent mode analysis of viscous shock-laden flows, wherein the nonlinear smoothness-based weighting is disabled during mode computations to recover a consistent linear operator and achieve close agreement with semi-analytic viscous modes while retaining WENO's shock-capturing capabilities for the underlying flow solution. Finally, conclusions are drawn in § 6, where we discuss the implications of our findings and suggest directions for future research.

2. Resolvent analysis

Resolvent analysis identifies the most responsive forcings and most receptive responses of a dynamical system under constant-frequency excitation. Consider the system of nonlinear partial differential equations describing the compressible, viscous flow within a given computational domain. The discretised flow governing equations may be written as

$$\frac{\mathrm{d}\boldsymbol{Q}}{\mathrm{d}t} = \boldsymbol{N}(\boldsymbol{Q}), \tag{2.1}$$

where $\boldsymbol{Q}$ is the flow solution and $\boldsymbol{N}$ is the discrete nonlinear differential operator. Linearisation of (2.1) for small perturbations $\boldsymbol{Q}' = \boldsymbol{Q} - \bar{\boldsymbol{Q}}$ to the base-flow $\bar{\boldsymbol{Q}}$ satisfying $\boldsymbol{N}(\bar{\boldsymbol{Q}}) = 0$ yields

$$\frac{\mathrm{d}\boldsymbol{Q}'}{\mathrm{d}t} = \boldsymbol{L}(\bar{\boldsymbol{Q}})\,\boldsymbol{Q}', \tag{2.2}$$

where $\boldsymbol{L}$ is the corresponding discrete linearised differential operator evaluated about the base-flow $\bar{\boldsymbol{Q}}$. Next, identification of the most responsive forcings and receptive responses of the dynamical system (2.2), requires the following modifications be considered:

$$\frac{\mathrm{d}\boldsymbol{Q}'}{\mathrm{d}t} = \boldsymbol{L}(\bar{\boldsymbol{Q}})\,\boldsymbol{Q}' + \boldsymbol{B}\boldsymbol{f}, \quad \boldsymbol{r} = \boldsymbol{C}\boldsymbol{Q}', \tag{2.3}$$

where the vector $\boldsymbol{f}$ contains zero-mean source terms of the continuity, momentum and energy equations, and represents an external forcing on the linearised, governing

https://doi.org/10.1017/jfm.2026.11255 Published online by Cambridge University Press

equations. The vector $\boldsymbol{r}$ represents the system's response, and the matrices $\boldsymbol{B}$ and $\boldsymbol{C}$ specify the inputs to and outputs from the system. Next, a Fourier-transformation of the previous equations, in the form

$$\boldsymbol{Q}'(\boldsymbol{x}, t) = \int_{-\infty}^{\infty} \hat{\boldsymbol{Q}}(\boldsymbol{x}, \omega) e^{i\omega t}\, d\omega, \tag{2.4}$$

yields a frequency domain system

$$\hat{\boldsymbol{r}} = \boldsymbol{C}\hat{\boldsymbol{Q}} = \boldsymbol{C}(i\omega\boldsymbol{I} - \boldsymbol{L})^{-1}\boldsymbol{B}\hat{\boldsymbol{f}} = \boldsymbol{C}\boldsymbol{R}(\omega)\boldsymbol{B}\hat{\boldsymbol{f}} = \boldsymbol{H}(\omega)\hat{\boldsymbol{f}}, \tag{2.5}$$

where $\boldsymbol{R}(\omega)$ is the resolvent operator (Schmid 2007) and $\boldsymbol{H}(\omega)$ is the frequency domain input–output operator relating the forcing ($\hat{\boldsymbol{f}}$) and response ($\hat{\boldsymbol{r}}$) modes. Next, a measure of the forcing and response mode energy is established through the introduction of positive definite norms $\boldsymbol{D_r} > 0$ and $\boldsymbol{D_f} > 0$, respectively. These are usually characterised by an inner product encompassing a weighted integral over the entire domain; $\langle \boldsymbol{a}, \boldsymbol{b}\rangle_{\boldsymbol{r}} = \boldsymbol{a}^H \boldsymbol{D_r} \boldsymbol{b} = \boldsymbol{a}^H \boldsymbol{N_r^H} \boldsymbol{N_r} \boldsymbol{b}$ and $\langle \boldsymbol{a}, \boldsymbol{b}\rangle_{\boldsymbol{f}} = \boldsymbol{a}^H \boldsymbol{D_f} \boldsymbol{b} = \boldsymbol{a}^H \boldsymbol{N_f^H} \boldsymbol{N_f} \boldsymbol{b}$, where $\boldsymbol{N_r}$ and $\boldsymbol{N_f}$ represent the Cholesky decomposition factors of the matrices $\boldsymbol{D_r}$ and $\boldsymbol{D_f}$, respectively. From these, the definition of a gain $\sigma(\omega)$, which represents the energy of the response corresponding to a unit energy forcing, follows as

$$\sigma^2(\omega) = \max_{\hat{\boldsymbol{f}}} \frac{\langle \hat{\boldsymbol{r}}, \hat{\boldsymbol{r}}\rangle_{\boldsymbol{r}}}{\langle \hat{\boldsymbol{f}}, \hat{\boldsymbol{f}}\rangle_{\boldsymbol{f}}} = \max \mathtt{svd}\left(\boldsymbol{N_r}\boldsymbol{H}(\omega)\boldsymbol{N_f^{-1}}\right). \tag{2.6}$$

As mentioned in (2.6), a singular value decomposition that incorporates the forcing and response norms, and the operator $\boldsymbol{H}(\omega)$, is then used to compute a set of optimal forcing and response modes. These modes may represent a low-ranked approximation of the forcing-response dynamics of the full system. Additionally, the forcing and response mode pairs are capable of providing the structural sensitivity of a system, such as to localised feedback in the flow. By considering perturbations $\mathrm{d}\boldsymbol{L}$ (in the linear limit) to the operator $\boldsymbol{L}$, the change in gain $\mathrm{d}\sigma$ (see Appendix D for derivation) can be evaluated as

$$\mathrm{d}\sigma = \mathrm{Re}\left(\hat{\boldsymbol{y}}^H (\boldsymbol{N_r}\boldsymbol{C}(\boldsymbol{R}(\omega)\,\mathrm{d}\boldsymbol{L}\boldsymbol{R}(\omega))\,\boldsymbol{B}\boldsymbol{N_f^{-1}})\,\hat{\boldsymbol{w}}/(\hat{\boldsymbol{y}}^H\hat{\boldsymbol{y}})\right), \tag{2.7}$$

where $\hat{\boldsymbol{r}} = \sigma \boldsymbol{N_r^{-1}}\hat{\boldsymbol{y}}$ and $\hat{\boldsymbol{f}} = \boldsymbol{N_f^{-1}}\hat{\boldsymbol{w}}$. These gain sensitivities can then be used to identify locations within the flow of sensor/actuator placement for flow control applications. In the next section, we begin with the inviscid problem, deriving the forward and adjoint Green's function operators, and constructing the zero-frequency resolvent operator.

3. Resolvent analysis in inviscid shock-laden flows

Building upon the foundational work of Giles *et al.* (1997) and Giles & Pierce (2001), who derived convergent adjoint solutions for inviscid shock-laden flows, we aim to extend these methodologies to a resolvent analysis framework. In their studies, it was demonstrated that the adjoint field exhibits a logarithmic singularity at the sonic point and maintains C^1 continuity across shocks when linear functionals are considered. However, Bodony & Fikl (2022) highlighted that, for quadratic functionals, many commonly used shock-capturing numerical methods fail to yield convergent adjoint solutions due to the inherent discontinuities introduced by shocks.

The present work seeks to bridge this gap by developing a semi-analytical resolvent calculation that can verify the effectiveness of numerical methods in capturing meaningful linearised operators in the presence of shocks or other discontinuities. Specifically, we

https://doi.org/10.1017/jfm.2026.11255 Published online by Cambridge University Press

focus on the quasi-one-dimensional Euler equations, which, despite their simplicity, capture the essential features of shock-laden flows in converging–diverging nozzles. This choice allows for a tractable analysis while still providing valuable insights applicable to more complex, multidimensional flows.

Our approach involves employing a Green's function methodology to derive resolvent solutions for the inviscid case. By constructing the forward and adjoint Green's function operators, we can account for the discontinuities introduced by shocks explicitly in the formulation. This enables us to examine the properties of the resolvent operator and its associated modes in shock-laden flows and to provide benchmarks against which numerical resolvent analyses can be validated.

3.1. *Inviscid quasi-one-dimensional flow equations*

The steady inviscid quasi-one-dimensional (quasi-1-D) equations representing the compressible flow through a converging–diverging nozzle are given as

$$\mathcal{R}(\boldsymbol{U}, h) = \frac{\mathrm{d}}{\mathrm{d}x}(\boldsymbol{F}h) - \frac{\mathrm{d}h}{\mathrm{d}x}\boldsymbol{P} = \boldsymbol{0}, \tag{3.1}$$

where

$$\boldsymbol{U} = \begin{bmatrix} \rho \\ \rho q \\ \rho E \end{bmatrix}, \quad \boldsymbol{F} = \begin{bmatrix} \rho q \\ \rho q^2 + p \\ \rho q H \end{bmatrix}, \quad \boldsymbol{P} = \begin{bmatrix} 0 \\ p \\ 0 \end{bmatrix}. \tag{3.2}$$

Here, ρ is the density, q is the velocity, p is the pressure, E is the total energy, H is the stagnation enthalpy and $h(x)$ represents the nozzle cross-sectional area as a function of axial position x. The system is closed by the equation of state for an ideal gas

$$H = E + \frac{p}{\rho} = \frac{\gamma}{\gamma - 1}\frac{p}{\rho} + \frac{1}{2}q^2. \tag{3.3}$$

Additionally, if the solution to the quasi-1-D equations contains a stationary discontinuity (at $x = x_s$), the Rankine–Hugoniot jump conditions are given by

$$[\![\boldsymbol{F}]\!]_{x_s^-}^{x_s^+} = 0. \tag{3.4}$$

3.2. *Forward Green's function operator*

To construct the Green's function operator $\boldsymbol{G}(x, \xi)$ for the forward linearised problem, the governing equations (3.1) are linearised about a steady base-flow $\boldsymbol{U}(x)$. The linearised operator $\boldsymbol{L}$ acting on a perturbation $\boldsymbol{u}(x)$ is defined as

$$\boldsymbol{L}\boldsymbol{u} = \frac{\mathrm{d}}{\mathrm{d}x}\left(h(x)\boldsymbol{A}(x)\boldsymbol{u}\right) - \frac{\mathrm{d}h}{\mathrm{d}x}\boldsymbol{B}(x)\boldsymbol{u}, \tag{3.5}$$

where

$$\boldsymbol{A}(x) = \frac{\partial \boldsymbol{F}}{\partial \boldsymbol{U}}, \quad \boldsymbol{B}(x) = \frac{\partial \boldsymbol{P}}{\partial \boldsymbol{U}}. \tag{3.6}$$

Next, three linearly independent homogeneous solutions $\hat{\boldsymbol{u}}_j(x)$ satisfying $\boldsymbol{L}\hat{\boldsymbol{u}}_j = \boldsymbol{0}$ are constructed. These solutions represent the fundamental modes of the linearised system.

To build the operator $\boldsymbol{G}(x, \xi)$ such that

$$\boldsymbol{u}(x) = \int_D \boldsymbol{G}(x, \xi)\, \boldsymbol{f}(\xi)\, d\xi, \tag{3.7}$$

https://doi.org/10.1017/jfm.2026.11255 Published online by Cambridge University Press

where $\boldsymbol{L}\boldsymbol{u}(x) = \boldsymbol{f}(x)$, a set of linearly independent piecewise solutions, composed of the homogeneous solutions $\hat{\boldsymbol{u}}_j$, is sought:

$$\boldsymbol{u}_i(x,\xi) = \begin{cases} \boldsymbol{u}_{L,i}(x) & \text{for } x < \xi, \\ \boldsymbol{u}_{R,i}(x) & \text{for } x > \xi, \end{cases} \tag{3.8}$$

where i enumerates the set of linearly independent piecewise solutions $\boldsymbol{u}_i(x,\xi)$, satisfying

$$\boldsymbol{L}\boldsymbol{u}_i(x,\xi) = \boldsymbol{f}_i(\xi)\delta(x-\xi), \tag{3.9}$$

$\boldsymbol{u}_{L,i}(x) = a_{L,i,j}\hat{\boldsymbol{u}}_j(x)$ and $\boldsymbol{u}_{R,i}(x) = a_{R,i,j}\hat{\boldsymbol{u}}_j(x)$ are linear combinations of the homogeneous solutions (here, summation is implied over repeated indices). The jump conditions for constants $a_{L,i,j}$ and $a_{R,i,j}$, in the solution $\boldsymbol{u}_i(x,\xi)$ at $x = \xi$, are determined by integrating the linearised equation across the singularity

$$\int_{\xi^-}^{\xi^+} \boldsymbol{L}\boldsymbol{u}_i(x,\xi)\,\mathrm{d}x = \boldsymbol{f}_i(\xi), \tag{3.10}$$

and choosing three linearly independent source vectors $\boldsymbol{f}_i(\xi)$; as described by Giles & Pierce (2001). Then, the Green's function operator is constructed using the vectors $\boldsymbol{u}_i(x,\xi)$ and $\boldsymbol{f}_i(\xi)$ as

$$\boldsymbol{G}(x,\xi) = (\boldsymbol{u}_1(x,\xi) \mid \boldsymbol{u}_2(x,\xi) \mid \boldsymbol{u}_3(x,\xi))\ \left(\boldsymbol{f}_1(\xi) \mid \boldsymbol{f}_2(\xi) \mid \boldsymbol{f}_3(\xi)\right)^{-1}, \tag{3.11}$$

where vertical lines indicate the partitioning of the row vector and array into three columns. Please refer to Giles & Pierce (2001) for explicit formulae.

3.3. *Adjoint Green's function operator*

Similar to the construction of the forward Green's function, the Green's function for the adjoint problem can be constructed using three linearly independent gradient functions ($\boldsymbol{g}_i$) and corresponding adjoint solutions ($\boldsymbol{v}_i$) such that $\boldsymbol{L}^\dagger\boldsymbol{v}_i(x,\eta) = \boldsymbol{g}_i(\eta)\delta(x-\eta)$. To accomplish this, similar to Giles & Pierce (2001), we define three objective functions J_i, as integrals of the pressure, temperature (T) and velocity, over the domain D:

$$J_1 = \int_D p(x)\,\mathrm{d}x, \quad J_2 = \int_D T(x)\,\mathrm{d}x, \quad J_3 = \int_D q(x)\,\mathrm{d}x. \tag{3.12}$$

The corresponding gradients ($\boldsymbol{g}_i(\eta) = \partial k_i(\eta)/\partial \boldsymbol{U}$; $\partial p/\partial \boldsymbol{U}$, $\partial T/\partial \boldsymbol{U}$ and $\partial q/\partial \boldsymbol{U}$) of the objective function integrands (k_i such that $J_i = \int_D k_i(x)\,\mathrm{d}x$) are then used to linearise the augmented nonlinear objective functional $J_{i,j}$ (similar to (2.2) of Giles & Pierce (2001)) as shown as

$$\begin{aligned} dJ_{i,j} = I_{i,j}(\xi,\eta) = \int_D \Bigg\{ & \boldsymbol{u}_j(x,\xi)\cdot\frac{\partial k_i(\eta)}{\partial \boldsymbol{U}}\delta(x-\eta) \\ & - k_i(\eta)\,\delta(x-\eta)\,\delta(x-x_s^+)\,\delta_j(\xi) \\ & + k_i(\eta)\,\delta(x-\eta)\,\delta(x-x_s^-)\,\delta_j(\xi) \Bigg\}\,\mathrm{d}x \end{aligned} \tag{3.13}$$

$$\begin{aligned} = {} & \boldsymbol{u}_j(\eta,\xi)\cdot\boldsymbol{g}_i(\eta) \\ & - k_i(\eta)\,\delta(\eta-x_s^+)\,\delta_j(\xi) \\ & + k_i(\eta)\,\delta(\eta-x_s^-)\,\delta_j(\xi), \end{aligned} \tag{3.14}$$

https://doi.org/10.1017/jfm.2026.11255 Published online by Cambridge University Press

where δ_j represents the linearised displacement of the shock location, and the indices i and j represent the choice of objective function and linearly independent piecewise solution $\boldsymbol{u}_j(x,\xi)$ (with associated $\boldsymbol{f}_j(\xi)\delta(x-\xi)$; corresponding to a jump in ρuh, H or p_0) used to compute the perturbation $I_{i,j}$, respectively. Then, the operator $(I_{i,1}(\xi,\eta) \mid I_{i,2}(\xi,\eta) \mid I_{i,3}(\xi,\eta))$, along with the adjoint form of the linearised objective function

$$I_{i,j}(\xi,\eta) = \int_D \boldsymbol{v}_i^T(x,\eta)\boldsymbol{f}_j(\xi)\delta(x-\xi)\,dx = \boldsymbol{v}_i^T(\xi,\eta)\boldsymbol{f}_j(\xi), \tag{3.15}$$

is used to evaluate

$$\boldsymbol{v}_i^T(\xi,\eta) = \left(I_{i,1}(\xi,\eta) \mid I_{i,2}(\xi,\eta) \mid I_{i,3}(\xi,\eta)\right)\ \left(\boldsymbol{f}_1(\xi) \mid \boldsymbol{f}_2(\xi) \mid \boldsymbol{f}_3(\xi)\right)^{-1}, \tag{3.16}$$

which is used to obtain the Green's function for the adjoint problem, as

$$\boldsymbol{G}^{\dagger}(x,\eta) = (\boldsymbol{v}_1(x,\eta) \mid \boldsymbol{v}_2(x,\eta) \mid \boldsymbol{v}_3(x,\eta))\ \left(\boldsymbol{g}_1(\eta) \mid \boldsymbol{g}_2(\eta) \mid \boldsymbol{g}_3(\eta)\right)^{-1}. \tag{3.17}$$

Furthermore, the adjoint solution $\boldsymbol{v}(x)$ corresponding to any given $\boldsymbol{g}(\eta)$ is then given by

$$\boldsymbol{v}(x) \overset{\text{def}}{=} \int_D \boldsymbol{G}^{\dagger}(x,\eta)\ \boldsymbol{g}(\eta)\,\mathrm{d}\eta, \tag{3.18}$$

and substituting (3.14), (3.16) and (3.17) into (3.18) (for a detailed derivation, please refer to Appendix I), we have

$$\begin{aligned}\boldsymbol{v}(x) = &\int_D \boldsymbol{W}^{-T}(x)\begin{bmatrix}\boldsymbol{u}_1(\eta,x)^H\\ \boldsymbol{u}_2(\eta,x)^H\\ \boldsymbol{u}_3(\eta,x)^H\end{bmatrix}\boldsymbol{g}(\eta)\,\mathrm{d}\eta\\ &- \boldsymbol{W}^{-T}(x)\begin{Bmatrix}\delta_1(x)\\ 0\\ \delta_3(x)\end{Bmatrix}\left[\left(p \mid T \mid q\right)\boldsymbol{T}^{-1}\,\boldsymbol{g}\right]_{x_s^-}^{x_s^+},\end{aligned} \tag{3.19}$$

where $\boldsymbol{W}(x) = (\boldsymbol{f}_1(x) \mid \boldsymbol{f}_2(x) \mid \boldsymbol{f}_3(x))$ and $\boldsymbol{T}(x) = (\boldsymbol{g}_1(x) \mid \boldsymbol{g}_2(x) \mid \boldsymbol{g}_3(x))$.

3.4. *Procedure to construct the zero-frequency resolvent modes*

As a first extension of Giles & Pierce (2001), we consider the zero frequency resolvent modes (forcing modes $\hat{\boldsymbol{f}}$ and response modes $\hat{\boldsymbol{r}}$). These are constructed by solving for the forcing $\hat{\boldsymbol{f}}$ that will maximise the gain σ using the Green's function operators of the forward and adjoint problems, which were derived in the previous subsections, as follows:

$$\sigma^2 = \max_{\hat{f}}\left(\frac{\langle\hat{\boldsymbol{r}},\hat{\boldsymbol{r}}\rangle}{\langle\hat{\boldsymbol{f}},\hat{\boldsymbol{f}}\rangle}\right) = \max_{\hat{f}}\left(\frac{\langle\boldsymbol{G}*\hat{\boldsymbol{f}},\boldsymbol{G}*\hat{\boldsymbol{f}}\rangle}{\langle\hat{\boldsymbol{f}},\hat{\boldsymbol{f}}\rangle}\right) \tag{3.20}$$

$$= \max_{\hat{f}}\left(\frac{\langle\hat{\boldsymbol{f}},\boldsymbol{G}^{\dagger}*\boldsymbol{G}*\hat{\boldsymbol{f}}\rangle}{\langle\hat{\boldsymbol{f}},\hat{\boldsymbol{f}}\rangle}\right). \tag{3.21}$$

A normalised power iteration method is used to solve the eigenvalue problem

$$\boldsymbol{G}^{\dagger} * \boldsymbol{G} * \hat{\boldsymbol{f}} = \sigma^2\hat{\boldsymbol{f}}, \tag{3.22}$$

where $*$ represents the convolution operation. We chose this iterative, matrix-free approach because it computes the action of the resolvent operator and its adjoint on state vectors without requiring the explicit formation and storage of the full resolvent matrix. This

https://doi.org/10.1017/jfm.2026.11255 Published online by Cambridge University Press

makes the method computationally efficient and scalable to problems with very fine grid resolutions or higher spatial dimensions, where the memory cost of the dense resolvent operator would be prohibitive. It should be noted, however, that for problems where the discrete operator is small enough to be stored in memory, a direct computation via a singular value decomposition (SVD) would be a more robust and preferable alternative. This produces a solution to the most-amplified-forcing ($\hat{\boldsymbol{f}}$) and most-receptive-response,

$$\hat{\boldsymbol{r}}(x) = \int_D \boldsymbol{G}(x, \xi)\, \hat{\boldsymbol{f}}(\xi)\, \mathrm{d}\xi, \tag{3.23}$$

mode corresponding to the linear system $\boldsymbol{L}\hat{\boldsymbol{r}} = \hat{\boldsymbol{f}}$. Equations (3.11), (3.17), (3.22) and (3.23) are the key results of this section whose details are now demonstrated.

3.5. *Zero-frequency resolvent analysis of shock-laden quasi-1-D flow*

In this section, the zero-frequency resolvent modes corresponding to steady flow through a duct of cross-section $h(x)$ governed by the quasi-one-dimensional Euler equations (3.1) are computed using the procedure described in § 3.4 and compared against the same modes computed using a finite volume method (FVM) fitted with the Jameson–Schmidt–Turkel (JST; Jameson (2017)) scheme.

3.5.1. *Inviscid base-flow solution*

Three steady quasi-1-D flows through a CD nozzle – one supersonic, one subsonic and the other shock-laden – are considered. The geometric definition of the CD nozzle is given by

$$h(x) = 2 - e^{-x^2/0.09}\ (-2 \leqslant x \leqslant 2). \tag{3.24}$$

This modification to the CD nozzle geometry, from the one used by Giles & Pierce (2001), was made to ensure that the geometry is C^2 smooth at every point over the domain ($-2 \leqslant x \leqslant 2$). In the case of the supersonic flow, the inlet is set to a non-dimensional (as per Giles & Pierce 2001) stagnation enthalpy $H_{in} = 4$, stagnation pressure $p_{0,in} = 2$ and Mach number $M_{in} = 3$. In the case of the subsonic flow, the inlet is set to the same stagnation conditions, but a different exit condition where the static pressure is $p_{out} = 1.98$. Finally, a flow with the same inlet conditions and the static pressure $p_{out} = 1.6$ is considered. This exit boundary condition generates a steady quasi-1-D flow that features a shock in the diverging section of the CD nozzle.

The isentropic flows are chosen to verify the derivation for the zero-frequency resolvent modes corresponding to the quasi-1-D flow through a CD nozzle, given in § 3.4, through comparison with numerical results. The shock-laden case is used to verify that a properly selected discrete numerical methodology (as shown by Lozano & Ponsin 2012) can converge to the verified zero-frequency resolvent mode solutions computed as per § 3.4, except at $x = x_s$.

3.5.2. *Resolvent modes of inviscid shock-free base flows*

The semi-analytic zero-frequency resolvent modes corresponding to the shock-free isentropic flows are computed by solving the eigenvalue problem that results when computing the SVD of the resolvent operator, as described in § 2. Figures 1, 2, 3 and 4, show the agreement between the resolvent solution obtained as described in §§ 2 and 3.4. As expected, no particular difficulties are encountered.

https://doi.org/10.1017/jfm.2026.11255 Published online by Cambridge University Press

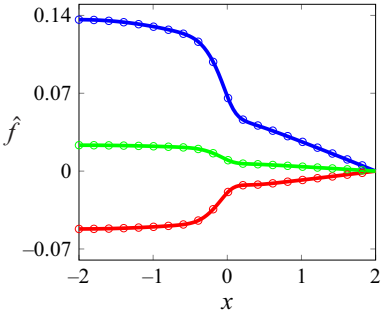


Figure 1. Match between forcing modes computed as per Giles & Pierce (2001) (solid lines) compared with a central FVM + JST based discrete (circles) implementation for supersonic isentropic flow through a CD nozzle.

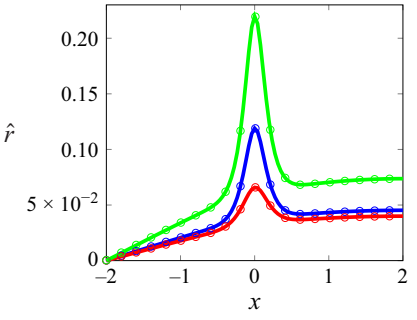


Figure 2. Match between response modes computed as per Giles & Pierce (2001) (solid lines) compared with a central FVM + JST based discrete (circles) implementation for supersonic isentropic flow through a CD nozzle.

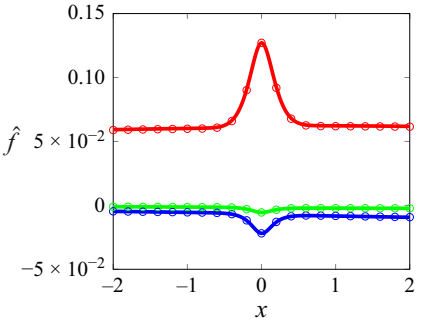


Figure 3. Match between forcing modes computed as per Giles & Pierce (2001) (solid lines) compared with a central FVM + JST based discrete (circles) implementation for subsonic isentropic flow through a CD nozzle.

3.5.3. *Adjoint and forward solutions of inviscid shock-laden base flows*

Building on works such as Lozano (2016) and Bodony & Fikl (2022), we use an inviscid linear finite volume discretization with JST dissipation (see Appendix A for details), implemented in a cell-centred finite volume method (FVM) framework. Following Lozano & Ponsin (2012), we modify the boundary residuals of both the forward and adjoint solvers so that the resulting discrete adjoint is simultaneously the algebraic adjoint

https://doi.org/10.1017/jfm.2026.11255 Published online by Cambridge University Press

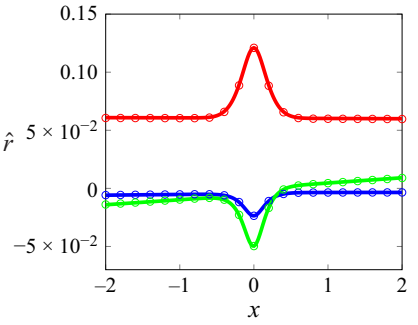


Figure 4. Match between response modes computed as per Giles & Pierce (2001) (solid lines) compared with a central FVM + JST based discrete (circles) implementation for subsonic isentropic flow through a CD nozzle.

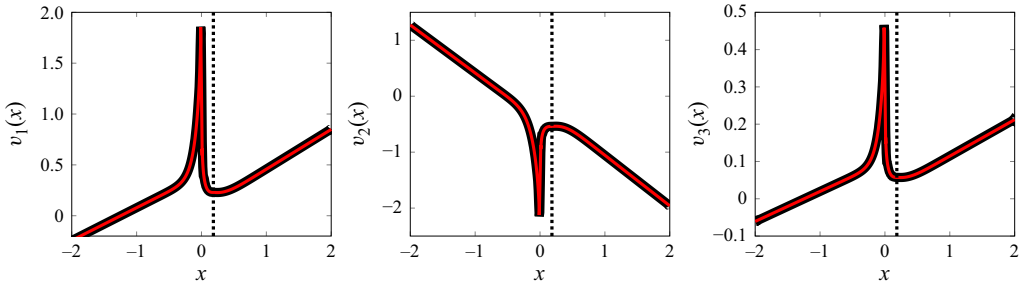


Figure 5. Converged adjoint mode solution (FVM + JST based implementation, represented as ▬) and solution as per Giles & Pierce (2001) (represented as ▬), corresponding to the transonic shock-laden flow (shock location is indicated by ▪▪▪▪) through a quasi-1-D flow through a CD nozzle.

of the discrete forward operator and a consistent discretisation of the continuous adjoint (including its boundary conditions), and the overall scheme is therefore dual consistent. The artificial dissipation terms, combining second- and fourth-order differences, are carefully constructed to ensure compatibility with both conservation laws and the adjoint system, while preserving energy stability and avoiding spurious oscillations. This dual consistency eliminates non-physical artefacts, ensures convergence of the adjoint solutions to the analytical adjoint as grid resolution increases and provides accurate treatment of internal boundaries like shocks, resulting in well-behaved and stable adjoint fields critical for sensitivity analysis and optimisation in compressible flows.

Figures 5 and 6 illustrate this by showing agreement between the numerical adjoint ($\boldsymbol{v}$) and forward ($\boldsymbol{u}$) solutions, and their respective analytic counterparts. This agreement is observed pointwise across the domain, except at the shock location ($x = x_s$). The analytic solutions are derived following the methodology outlined by Giles & Pierce (2001) and the Green's function approach described in the preceding sections, tailored for shock-laden base flows, a specific gradient $\boldsymbol{g}$ and forcing $\boldsymbol{f}$.

3.5.4. *Resolvent solutions of inviscid shock-laden base flows*

This section investigates a significant disagreement between resolvent solutions obtained through numerical and semi-analytic approaches when shock waves are present in the base flow. Despite successfully computing pointwise (excluding the shock location) convergent adjoint and forward solutions using the numerical method outlined in § 3.5.3, and the

https://doi.org/10.1017/jfm.2026.11255 Published online by Cambridge University Press

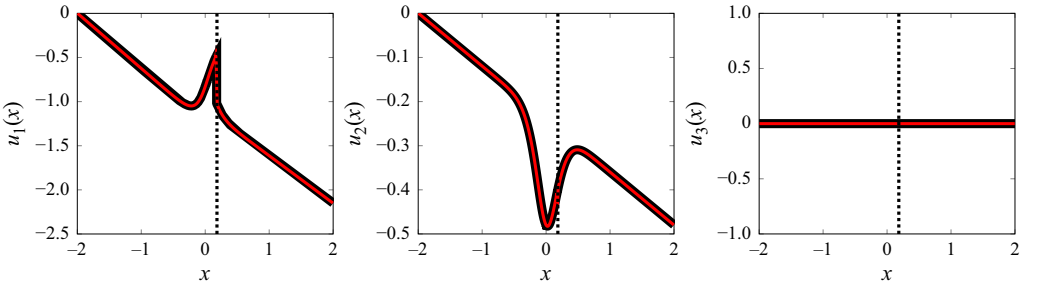


Figure 6. Pointwise converged (except at $x = x_s$) forward mode solution (FVM + JST based implementation represented as ▬) and solution as per Giles & Pierce (2001) (represented as ▬) corresponding to the transonic shock-laden flow (shock location is indicated by ▪▪▪) through a quasi-1-D flow through a CD nozzle.

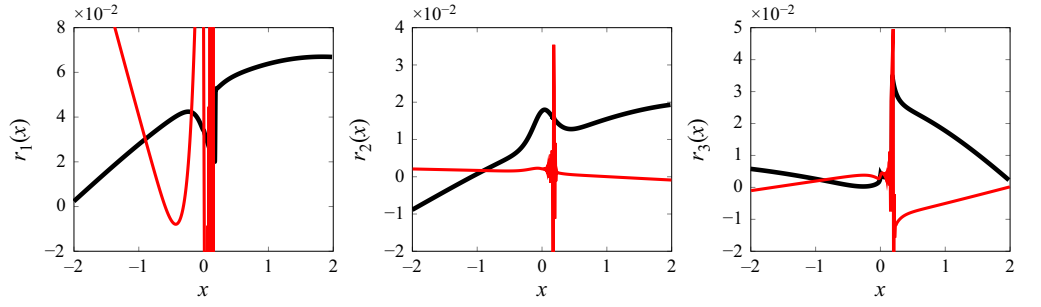


Figure 7. Comparison between the resolvent modes computed using (3.20) (represented as ▬) and using a FVM + JST based implementation (represented as ▬).

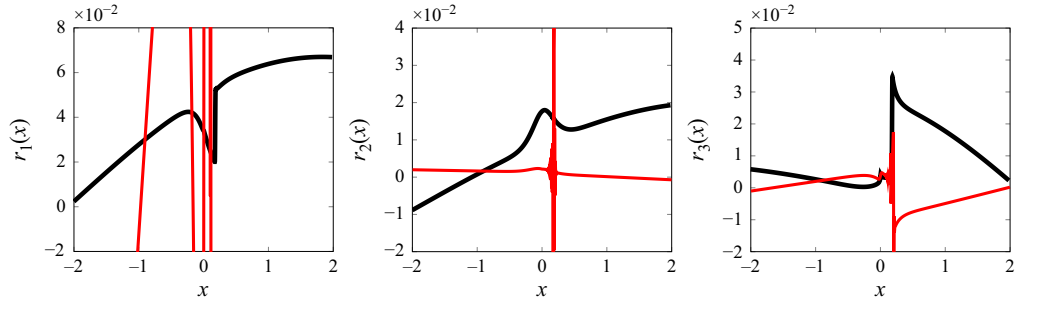


Figure 8. Comparison between the resolvent modes computed using (3.20) (represented as ▬) and using a FVM + JST based implementation (represented as ▬) with increased resolution ($\Delta x = 2/3\ \Delta x_{coarse}$, where Δx_{coarse} corresponds to the uniform grid spacing in figure 7).

linear operator formulation in (2.5), significant challenges arise when attempting to resolve the resolvent modes. Figures 7 and 8 reveals a clear misalignment between the leading semi-analytic and numerical resolvent modes.

To understand the origin of these discrepancies and foreshadowing the developments in § 4.1, we augmented the numerical method by solving the viscous equations, removing the JST model and directly resolving the shock (see Appendix C for details). For small enough viscosity ($\mu \leqslant 5 \times 10^{-3}$), the direct-resolution approach successfully reproduces the converged (including the shock region) adjoint and forward solutions from the inviscid

https://doi.org/10.1017/jfm.2026.11255 Published online by Cambridge University Press

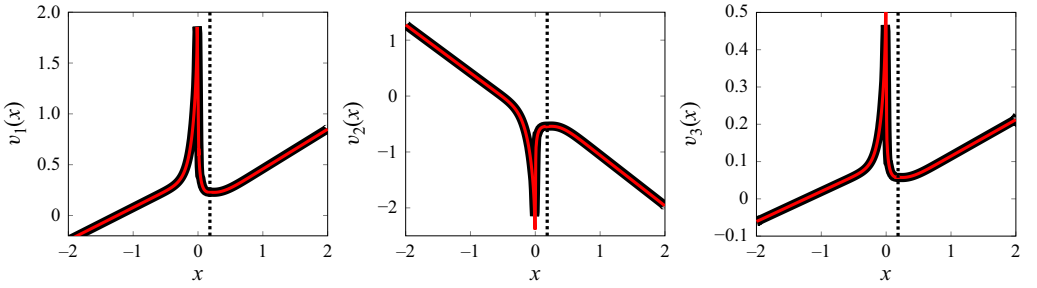


Figure 9. Converged adjoint mode solution (FVM + viscous-dissipation based implementation, represented as ▬) and solution as per Giles & Pierce (2001) (represented as ▬), corresponding to the transonic shock-laden flow (shock location is indicated by ▪▪▪) through a quasi-1-D flow through a CD nozzle.

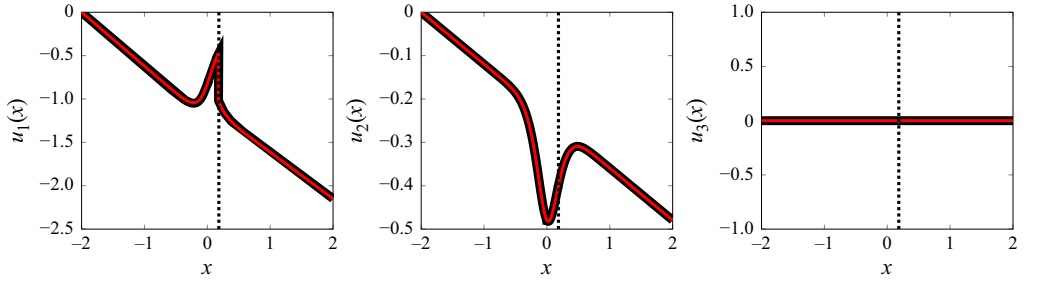


Figure 10. Pointwise converged (except at $x = x_s$) forward mode solution (FVM + viscous-dissipation based implementation represented as ▬) and solution as per Giles & Pierce (2001) (represented as ▬) corresponding to the transonic shock-laden flow (shock location is indicated by ▪▪▪) through a quasi-1-D flow through a CD nozzle.

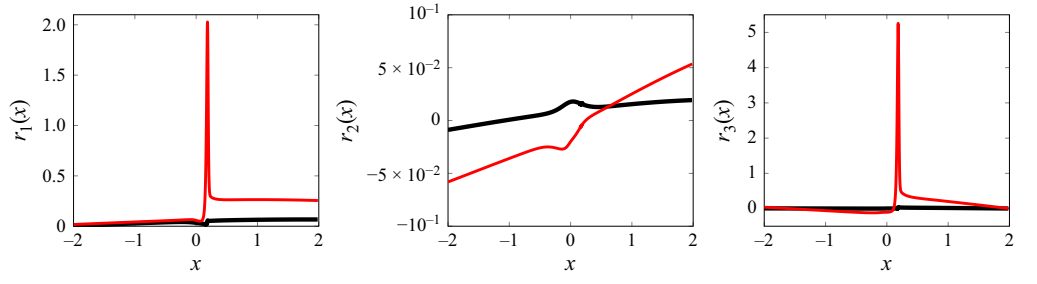


Figure 11. Comparison between the resolvent modes computed using (3.20) (represented as ▬) and using a FVM + viscous-dissipation ($\mu = 5 \times 10^{-3}$) based implementation (represented as ▬).

theory, as demonstrated in figures 9 and 10, respectively. However, this alternative implementation still does not fully reconcile the differences between the analytic and numerical resolvent results, as demonstrated in figure 11 for the dominant response mode.

We emphasise that a detailed comparison between the JST scheme and a physically viscous formulation is not the objective here. The key result is that the inviscid semi-analytical resolvent captures the system's resolvent response only away from the shock discontinuity; it does not account for the response at the shock itself and therefore cannot deliver the complete resolvent picture for shock-laden base flows. Consistent with this interpretation, we used the $\boldsymbol{C}$ operator from (2.3) to remove the shock from the output

https://doi.org/10.1017/jfm.2026.11255 Published online by Cambridge University Press

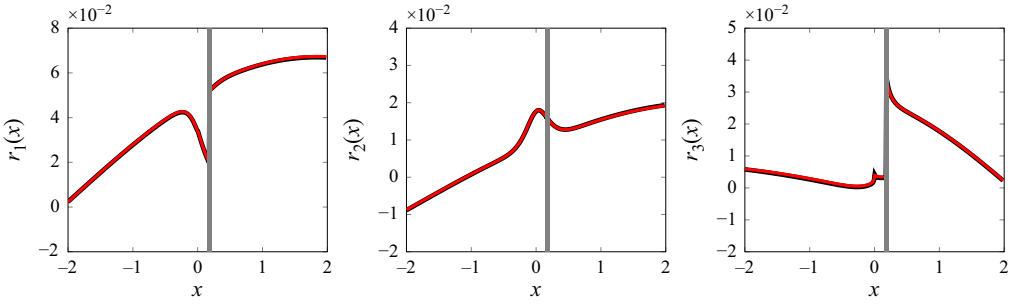


Figure 12. Comparison between the resolvent modes computed using (3.20) (represented as ▬) and using an FVM + viscous-dissipation based implementation with a mask (represented as ▬) over the spatial location of the shock (represented as ▬).

space – i.e. to exclude it from the norm used to measure the response and forcing modes (and hence, from the gain σ in (2.6)). With $\boldsymbol{C} \neq \boldsymbol{I}$, the agreement between the viscous-numerical and inviscid–semi-analytical resolvent modes improves markedly, as shown in figure 12. This result demonstrates that once the shock contribution is excluded from the norm, the viscous-numerical and inviscid-semi-analytical answers coincide, confirming that the inviscid model accurately captures the system's dynamics away from the shock while providing an incomplete description of the full resolvent response that includes the shock.

4. Resolvent analysis in viscous shock-laden flows

In the preceding semi-analytical analysis of inviscid shock-laden flows, the shock was treated as a discontinuity – a sudden jump in flow properties – without considering its internal structure or the possibility of forcing and responding directly at the shock location. While this approach captures some aspects of the flow's linear dynamics, it overlooks the impact of the shock's internal structure on the resolvent operator and the associated sensitivities.

To address this limitation, we extend the Green's function methodology to incorporate viscous effects, allowing the shock to be modelled as a continuous, albeit thin, region with strong gradients. This viscous extension enables the semi-analytic approach to account for the finite thickness of the shock and the associated viscous dissipation, which are essential for accurately capturing the flow's response to disturbances at and around the shock.

By incorporating viscosity, we can resolve discrepancies observed between numerical and semi-analytic resolvent solutions seen in the inviscid analyses. The viscous Green's function operators for both the forward and adjoint problems are derived, taking into account the additional terms introduced by viscous stresses and heat conduction, and provides a more comprehensive benchmark for evaluating numerical schemes, particularly those recommended by Bodony & Fikl (2022), ensuring that they capture the correct physical behaviour in the presence of shocks.

4.1. *Viscous quasi-one-dimensional flow equations*

To develop the viscous extension of the Green's function approach to resolvent mode computation, the viscous quasi-1-D equations considered in this study are

$$\mathcal{R}_{viscous}(\boldsymbol{U}, h) = \frac{\mathrm{d}}{\mathrm{d}x}(h\boldsymbol{F}) + \frac{\mathrm{d}}{\mathrm{d}x}\left(h\frac{\mathrm{d}}{\mathrm{d}x}(\boldsymbol{F}_{v,1})\right) + \frac{\mathrm{d}h}{\mathrm{d}x}\frac{\mathrm{d}}{\mathrm{d}x}(\boldsymbol{F}_{v,2}) - \frac{\mathrm{d}h}{\mathrm{d}x}\boldsymbol{P} = \boldsymbol{0}, \quad (4.1)$$

https://doi.org/10.1017/jfm.2026.11255 Published online by Cambridge University Press

where $\boldsymbol{U}$, $\boldsymbol{F}$, $\boldsymbol{P}$, H and $h(x)$ have the same definitions as in (3.2). Additionally, the viscous fluxes are defined as

$$\boldsymbol{F}_{v,1} = \begin{bmatrix} 0 \\ -\dfrac{4\mu q}{3} \\ -\dfrac{2\mu q^2}{3} - \dfrac{c_p \mu T}{Pr} \end{bmatrix}, \quad \boldsymbol{F}_{v,2} = \begin{bmatrix} 0 \\ \dfrac{4\mu q}{3} \\ 0 \end{bmatrix}, \tag{4.2}$$

and the terms μ, c_p and Pr are the dynamic viscosity, specific heat at constant pressure and the Prandtl number of the fluid.

4.2. *Viscous linear forward operator and basis solutions*

Starting with these viscous quasi-1-D nonlinear equations, the corresponding viscous linear forward problem is given by

$$\boldsymbol{L}_{viscous}\boldsymbol{u} = \frac{\mathrm{d}}{\mathrm{d}x}\left(h\frac{\partial \boldsymbol{F}}{\partial \boldsymbol{U}}\,\boldsymbol{u}\right) + \frac{\mathrm{d}}{\mathrm{d}x}\left(h\frac{\mathrm{d}}{\mathrm{d}x}\left(\frac{\partial \boldsymbol{F}_{v,1}}{\partial \boldsymbol{U}}\,\boldsymbol{u}\right)\right) + \frac{\mathrm{d}h}{\mathrm{d}x}\frac{\mathrm{d}}{\mathrm{d}x}\left(\frac{\partial \boldsymbol{F}_{v,2}}{\partial \boldsymbol{U}}\,\boldsymbol{u}\right) - \frac{\mathrm{d}h}{\mathrm{d}x}\frac{\partial \boldsymbol{P}}{\partial \boldsymbol{U}}\boldsymbol{u}. \tag{4.3}$$

Using $\boldsymbol{L}_{viscous}$, similar to Giles & Pierce (2001), piece-wise homogeneous ($\boldsymbol{L}_{viscous}\,\hat{\boldsymbol{u}}_i(x) = \boldsymbol{0}$) forward solutions $\boldsymbol{u}(x,\xi)$ that satisfy

$$\int_D \boldsymbol{L}_{viscous}\,\boldsymbol{u}(x,\xi)\,\mathrm{d}\xi = \int_D \delta(x-\xi)\,\boldsymbol{f}(\xi)\,\mathrm{d}\xi \tag{4.4}$$

can be constructed as follows:

$$\begin{aligned} \boldsymbol{u}(x,\xi) = a\mathscr{H}(x-\xi)\,\underbrace{\left(\frac{1}{h(x)}\frac{\partial \boldsymbol{U}}{\partial m}\bigg|_{H,q} + c_m(x)\,\frac{\partial \boldsymbol{U}}{\partial q}\bigg|_{m,H}\right)}_{\hat{\boldsymbol{u}}_1(x)} \\ + b\mathscr{H}(x-\xi)\,\underbrace{\left(\frac{\partial \boldsymbol{U}}{\partial H}\bigg|_{m,q} + c_H(x)\,\frac{\partial \boldsymbol{U}}{\partial q}\bigg|_{m,H}\right)}_{\hat{\boldsymbol{u}}_2(x)} \\ + c\mathscr{H}(-(x-\xi))\,\underbrace{\left(\frac{1}{h(x)}\frac{\partial \boldsymbol{U}}{\partial m}\bigg|_{H,q} + c_q(x)\,\frac{\partial \boldsymbol{U}}{\partial q}\bigg|_{m,H}\right)}_{\hat{\boldsymbol{u}}_3(x)}, \end{aligned} \tag{4.5}$$

where $\mathscr{H}(x-\xi)$ is the Heaviside step function, a and b represent uniform perturbations since the nonlinear quasi-1-D equations ensure that mass flux ($mh = \rho q h$) and stagnation enthalpy (when $Pr = 3/4$) remain constant along the CD nozzle. The unsubscripted variable c is a uniform amplitude term and the functions $c_{\{m,H,q\}}(x)$ represent the non-uniform velocity field perturbations that ensure the homogeneity equations $\boldsymbol{L}_{viscous}\hat{\boldsymbol{u}}_i(x) = \boldsymbol{0}$ are satisfied.

4.3. *Viscous linear adjoint equations and operator*

The adjoint equations and operator can be derived by considering the augmented nonlinear objective function J, where the adjoint solution $\boldsymbol{v}$ enforces the differential flow constraints,

$$J = \int_D p\,\mathrm{d}x - \int_D \boldsymbol{v}^T \cdot \mathcal{R}_{viscous}\,\mathrm{d}x. \tag{4.6}$$

https://doi.org/10.1017/jfm.2026.11255 Published online by Cambridge University Press

Similar to Giles & Pierce (2001), we choose the objective function to be the integral of pressure along the duct. Linearising this with respect to perturbations in the flow solution $\boldsymbol{u}$ gives $dJ = I$ as

$$I = \int_D \left\{ \boldsymbol{v}^T \cdot \boldsymbol{f} - \left(\boldsymbol{v}^T \cdot (\boldsymbol{L}_{viscous}\, \boldsymbol{u}) - \left(\frac{\partial p}{\partial \boldsymbol{U}} \right)^T \cdot \boldsymbol{u} \right) \right\} \mathrm{d}x. \tag{4.7}$$

Integration by parts is used (see Appendix E for details) to transfer the differential operator $\boldsymbol{L}_{viscous}$ from $\boldsymbol{u}$ to the variable $\boldsymbol{v}$ as shown as follows, starting with $\boldsymbol{A} = \partial \boldsymbol{F}/\partial \boldsymbol{U}$, $\boldsymbol{C}_1 = \partial \boldsymbol{F}_{v,1}/\partial \boldsymbol{U}$, $\boldsymbol{C}_2 = \partial \boldsymbol{F}_{v,2}/\partial \boldsymbol{U}$, $\boldsymbol{B} = \partial \boldsymbol{P}/\partial \boldsymbol{U}$ and $\boldsymbol{g} = \partial p/\partial \boldsymbol{U}$, to yield

$$\begin{aligned} I = \int_D \boldsymbol{v}^T \cdot \boldsymbol{f}\, \mathrm{d}x - \Bigg[& \boldsymbol{v}^T \cdot (h\boldsymbol{A}\boldsymbol{u}) - \boldsymbol{v}^T \cdot \left(h \frac{\mathrm{d}}{\mathrm{d}x} \left(\boldsymbol{C}_1 \boldsymbol{u} \right) \right) + \frac{\mathrm{d}\boldsymbol{v}^T}{\mathrm{d}x} \cdot \left(h \boldsymbol{C}_1 \boldsymbol{u} \right) \\ & - \left(\frac{\mathrm{d}h}{\mathrm{d}x} \boldsymbol{v} \right)^T \cdot \left(\boldsymbol{C}_2 \boldsymbol{u} \right) \Bigg]_{x=x_{inlet}}^{x=x_{outlet}} - \int_D \boldsymbol{u}^T \cdot \Bigg(- h\boldsymbol{A}^T \frac{\mathrm{d}\boldsymbol{v}}{\mathrm{d}x} + \boldsymbol{C}_1^T \frac{\mathrm{d}}{\mathrm{d}x} \left(h \frac{\mathrm{d}\boldsymbol{v}}{\mathrm{d}x} \right) \\ & - \boldsymbol{C}_2^T \frac{\mathrm{d}}{\mathrm{d}x} \left(\frac{\mathrm{d}h}{\mathrm{d}x} \boldsymbol{v} \right) - \frac{\mathrm{d}h}{\mathrm{d}x} \boldsymbol{B}^T \boldsymbol{v} - \frac{\partial p}{\partial \boldsymbol{U}} \Bigg) \mathrm{d}x. \end{aligned} \tag{4.8}$$

Therefore, given the boundary conditions from (4.8) and the requirement that

$$I = \int_D \boldsymbol{u}^T \cdot \boldsymbol{g}\, \mathrm{d}x = \int_D \boldsymbol{v}^T \cdot \boldsymbol{f}\, \mathrm{d}x, \tag{4.9}$$

the viscous adjoint equation, with adjoint operator $\boldsymbol{L}^{\dagger}_{viscous}$ and the gradient $\boldsymbol{g} = \partial p/\partial \boldsymbol{U}$), is given by

$$\boldsymbol{L}^{\dagger}_{viscous} \boldsymbol{v} - \boldsymbol{g} = -h\boldsymbol{A}^T \frac{\mathrm{d}\boldsymbol{v}}{\mathrm{d}x} + \boldsymbol{C}_1^T \frac{\mathrm{d}}{\mathrm{d}x} \left(h \frac{\mathrm{d}\boldsymbol{v}}{\mathrm{d}x} \right) - \boldsymbol{C}_2^T \frac{\mathrm{d}}{\mathrm{d}x} \left(\frac{\mathrm{d}h}{\mathrm{d}x} \boldsymbol{v} \right) - \frac{\mathrm{d}h}{\mathrm{d}x} \boldsymbol{B}^T \boldsymbol{v} - \frac{\partial p}{\partial \boldsymbol{U}}. \tag{4.10}$$

4.4. *Viscous adjoint solutions corresponding to a specific gradient*

The adjoint basis solutions can be computed by starting with (4.9), which represents the linearised objective function, the impulse forcing ($\boldsymbol{f}(\xi)\delta(x-\xi)$) such that

$$\boldsymbol{L}_{viscous}\, \boldsymbol{u}(x, \xi) = \boldsymbol{f}(\xi)\delta(x - \xi) \tag{4.11}$$

and

$$I(\xi) = \int_D \boldsymbol{g}^T \cdot \boldsymbol{u}(x, \xi)\, \mathrm{d}x - \int_D \boldsymbol{v}^T \cdot (\boldsymbol{L}_{viscous}\, \boldsymbol{u}(x, \xi) - \boldsymbol{f}(\xi)\delta(x - \xi))\, \mathrm{d}x. \tag{4.12}$$

Next, (4.12) can be transformed to a form similar to (4.8) as shown later, using another integration by parts procedure (see Appendix F for details), assuming $\boldsymbol{L}^{\dagger}_{viscous}\boldsymbol{v} - \boldsymbol{g} = \boldsymbol{0}$ and that the adjoint solutions satisfy the adjoint boundary conditions, then together with (4.11), we have

$$I(\xi) = \int_D \boldsymbol{v}^T(x) \cdot \{\boldsymbol{L}_{viscous}\, \boldsymbol{u}(x, \xi)\}\, \mathrm{d}x \tag{4.13}$$

$$\begin{aligned} = \Bigg\{ & \boldsymbol{v}^T(x) \cdot \left(h(x) \boldsymbol{A} \hat{\boldsymbol{p}}_1(x) \right) + \boldsymbol{v}^T(x) \cdot \left(h(x) \frac{\mathrm{d}}{\mathrm{d}x} \left(\boldsymbol{C}_1 \hat{\boldsymbol{p}}_1(x) \right) \right) \\ & + \boldsymbol{v}^T(x) \cdot \left(\frac{\mathrm{d}h(x)}{\mathrm{d}x} \boldsymbol{C}_2 \hat{\boldsymbol{p}}_1(x) \right) - \frac{\mathrm{d}\boldsymbol{v}^T(x)}{\mathrm{d}x} \cdot \left(h(x) \boldsymbol{C}_1 \hat{\boldsymbol{p}}_1(x) \right) \Bigg\} \Bigg|_{x=\xi} + BCs, \end{aligned} \tag{4.14}$$

https://doi.org/10.1017/jfm.2026.11255 Published online by Cambridge University Press

where the solution $\boldsymbol{u}(x,\xi)$ is assumed to have the form $H(x-\xi)\hat{\boldsymbol{p}}_1(x)+\hat{\boldsymbol{p}}_2(x)$, both $\hat{\boldsymbol{p}}_{i=1,2}$ are homogeneous solutions that satisfy $\boldsymbol{L}_{viscous}\hat{\boldsymbol{p}}_i=\boldsymbol{0}$ and BCs are the boundary conditions that emerge as a consequence of the integration by parts procedure; see Appendix F for details. Furthermore, the boundary conditions are satisfied for all ξ (on account of the properly constructed solutions $\boldsymbol{u}(x,\xi)$) and we have the equation

$$I(\xi)=\boldsymbol{v}^T(\xi)\cdot\left(h(\xi)\boldsymbol{A}\hat{\boldsymbol{p}}_1(\xi)+h(\xi)\,\frac{\mathrm{d}}{\mathrm{d}\xi}\big(\boldsymbol{C}_1\hat{\boldsymbol{p}}_1(\xi)\big)+\frac{\mathrm{d}h(\xi)}{\mathrm{d}\xi}\boldsymbol{C}_2\hat{\boldsymbol{p}}_1(\xi)\right)$$
$$-\frac{\mathrm{d}\boldsymbol{v}^T(\xi)}{\mathrm{d}\xi}\cdot\big(h(\xi)\boldsymbol{C}_1\hat{\boldsymbol{p}}_1(\xi)\big). \tag{4.15}$$

In the next section, we discuss how solutions to (4.15) are used to compute the adjoint Green's function operator.

4.5. *Viscous adjoint Green's function operator*

Starting with (4.15) from the previous section with $\boldsymbol{u}_j(x,\xi)=\mathscr{H}(x-\xi)\hat{\boldsymbol{u}}_j(x)$ and similar to (3.13), we consider the objective function perturbation $I_{i,j}(\xi,\eta)$ as follows:

$$\begin{aligned}I_{i,j}(\xi,\eta)&=\int_D\big\{\boldsymbol{g}_i^T(\eta)\,\delta(x-\eta)\big\}\cdot\boldsymbol{u}_j(x,\xi)\,\mathrm{d}x\\&=\boldsymbol{v}_i^T(\xi,\eta)\cdot\big(h(\xi)\boldsymbol{A}\hat{\boldsymbol{u}}_j(\xi)+h(\xi)\frac{\mathrm{d}}{\mathrm{d}\xi}\big(\boldsymbol{C}_1\hat{\boldsymbol{u}}_j(\xi)\big)\\&\quad+\frac{\mathrm{d}h(\xi)}{\mathrm{d}\xi}\,\boldsymbol{C}_2\hat{\boldsymbol{u}}_j(\xi)\big)-\frac{\partial\boldsymbol{v}_i^T(\xi,\eta)}{\partial\xi}\cdot\big(h(\xi)\boldsymbol{C}_1\hat{\boldsymbol{u}}_j(\xi)\big),\end{aligned} \tag{4.16}$$

such that

$$\begin{aligned}\boldsymbol{g}_i^T(\eta)\cdot\boldsymbol{u}_j(\eta,\xi)=\boldsymbol{v}_i^T(\xi,\eta)\cdot\Big\{&h(\xi)\boldsymbol{A}\hat{\boldsymbol{u}}_j(\xi)\\&+h(\xi)\,\frac{\mathrm{d}}{\mathrm{d}\xi}\big(\boldsymbol{C}_1\hat{\boldsymbol{u}}_j(\xi)\big)+\frac{\mathrm{d}h(\xi)}{\mathrm{d}\xi}\boldsymbol{C}_2\hat{\boldsymbol{u}}_j(\xi)\Big\}\\&-\frac{\partial\boldsymbol{v}_i^T(\xi,\eta)}{\partial\xi}\cdot\big(h(\xi)\boldsymbol{C}_1\hat{\boldsymbol{u}}_j(\xi)\big).\end{aligned} \tag{4.17}$$

Upon solving (see Appendix H for details) (4.17) for $\boldsymbol{v}_i(\xi,\eta)$ for a given gradient $\boldsymbol{g}_i(\eta)$, the viscous adjoint Green's function operator $\boldsymbol{G}^{\dagger}_{viscous}(x,\eta)$ can be computed, by first setting the dummy variable ξ to x for convenience, and then similar to (3.17), we have

$$\boldsymbol{G}^{\dagger}_{viscous}(x,\eta)=(\boldsymbol{v}_1(x,\eta)\mid\boldsymbol{v}_2(x,\eta)\mid\boldsymbol{v}_3(x,\eta))\cdot\big(\boldsymbol{g}_1(\eta)\mid\boldsymbol{g}_2(\eta)\mid\boldsymbol{g}_3(\eta)\big)^{-1}. \tag{4.18}$$

4.6. *Viscous forward Green's function operator*

Starting with equations (4.12), (4.13), the forward solutions $\tilde{\boldsymbol{u}}_i(x,\xi)$ such that

$$\boldsymbol{L}_{viscous}\tilde{\boldsymbol{u}}_i(x,\xi)=\hat{\boldsymbol{f}}_i(\xi)\delta(x-\xi) \tag{4.19}$$

and the adjoint solutions $\boldsymbol{v}_j(x,\eta)$ such that

$$\boldsymbol{L}^{\dagger}_{viscous}\boldsymbol{v}_j(x,\eta)=\boldsymbol{g}_j(\eta)\delta(x-\eta), \tag{4.20}$$

https://doi.org/10.1017/jfm.2026.11255 Published online by Cambridge University Press

and using (4.9), we have

$$\int_D \delta(x-\eta)\boldsymbol{g}_j^T(\eta)\cdot\tilde{\boldsymbol{u}}_i(x,\xi)\,\mathrm{d}x = \int_D \boldsymbol{v}_j^T(x,\eta)\cdot\hat{\boldsymbol{f}}_i(\xi)\delta(x-\xi)\,\mathrm{d}x \tag{4.21}$$

$$\Rightarrow \tilde{\boldsymbol{u}}_i(\eta,\xi) = (\boldsymbol{g}_1(\eta),\boldsymbol{g}_2(\eta),\boldsymbol{g}_3(\eta))^{-T}\cdot(\boldsymbol{v}_1(\xi,\eta),\boldsymbol{v}_2(\xi,\eta),\boldsymbol{v}_3(\xi,\eta))^T\cdot\hat{\boldsymbol{f}}_i(\xi), \tag{4.22}$$

and replacing the dummy variable η with x, we have

$$\tilde{\boldsymbol{u}}_i(x,\xi) = (\boldsymbol{g}_1(x),\boldsymbol{g}_2(x),\boldsymbol{g}_3(x))^{-T}\cdot(\boldsymbol{v}_1(\xi,x),\boldsymbol{v}_2(\xi,x),\boldsymbol{v}_3(\xi,x))^T\cdot\hat{\boldsymbol{f}}_i(\xi). \tag{4.23}$$

Next, three linearly independent vectors $\hat{\boldsymbol{f}}_i$ must be computed. This can be accomplished by considering the basis vectors $\boldsymbol{u}_i(x,\xi) = H(x-\xi)\hat{\boldsymbol{u}}_i(x)$ (with $\boldsymbol{L}_{viscous}\hat{\boldsymbol{u}}_i = \boldsymbol{0}$) and evaluating the following equation to compute the corresponding $\hat{\boldsymbol{f}}_i$ (see Appendix G for details):

$$\begin{aligned}\hat{\boldsymbol{f}}_i(x) = h(x)\frac{\partial \boldsymbol{F}}{\partial \boldsymbol{U}}\hat{\boldsymbol{u}}_i(x) + h(x)\frac{\mathrm{d}}{\mathrm{d}x}\left(\frac{\partial \boldsymbol{F}_{v,1}}{\partial \boldsymbol{U}}\hat{\boldsymbol{u}}_i(x)\right)\\ +\frac{\mathrm{d}}{\mathrm{d}x}\left[h(x)\left(\frac{\partial \boldsymbol{F}_{v,1}}{\partial \boldsymbol{U}}\hat{\boldsymbol{u}}_i(x)\right)\right] + \frac{\mathrm{d}h}{\mathrm{d}x}\left(\frac{\partial \boldsymbol{F}_{v,2}}{\partial \boldsymbol{U}}\hat{\boldsymbol{u}}_i(x)\right).\end{aligned} \tag{4.24}$$

It is important to note that the equation

$$\int_D \boldsymbol{L}_{viscous}\boldsymbol{u}_i(x,\xi)\,dx = \int_D \hat{\boldsymbol{f}}_i(\xi)\delta(x-\xi)\,dx \tag{4.25}$$

is not necessarily the same as (4.19), and hence the solutions $\boldsymbol{u}_i(x,\xi)$ and $\tilde{\boldsymbol{u}}_i(x,\xi)$ can differ. Finally, the viscous forward Green's function operator can now be constructed as follows:

$$\boldsymbol{G}_{viscous}(x,\xi) = (\tilde{\boldsymbol{u}}_1(x,\xi),\tilde{\boldsymbol{u}}_2(x,\xi),\tilde{\boldsymbol{u}}_3(x,\xi))\cdot(\hat{\boldsymbol{f}}_1(\xi),\hat{\boldsymbol{f}}_2(\xi),\hat{\boldsymbol{f}}_3(\xi))^{-1}. \tag{4.26}$$

4.7. *Resolvent solutions corresponding to viscous shock-laden base flows*

Similar to the inviscid case, the viscous ($\mu > 0$) zero-frequency resolvent modes corresponding to the shock-laden flows are computed by solving the eigenvalue problem that originates when computing the SVD of the resolvent operator $\boldsymbol{R}_{viscous}$, using the numerical approach given by

$$\boldsymbol{R}_{viscous}^{\dagger}\boldsymbol{R}_{viscous}\boldsymbol{f} = \sigma^2\boldsymbol{f} \quad \text{and} \quad \boldsymbol{r} = \boldsymbol{R}_{viscous}\boldsymbol{f}, \tag{4.27}$$

converge to the modes computed using the semi-analytic Green's function approach with the viscous extension

$$\boldsymbol{G}_{viscous}^{\dagger} * \boldsymbol{G}_{viscous} * \boldsymbol{f} = \sigma^2\boldsymbol{f} \quad \text{and} \quad \boldsymbol{r} = \boldsymbol{G}_{viscous} * \boldsymbol{f} \tag{4.28}$$

when shock-laden base-flows are considered, as shown in figures 13 and 14. Unlike classic convective instabilities where forcing and response are significantly separated, here the energy amplification is concentrated within the shock structure itself. However, this spatial overlap does not imply weak non-normality. On the contrary, the operator remains highly non-normal. The non-orthogonality of the eigenmodes arises not from large-scale spatial displacement, but from the subtle yet crucial misalignment in the modal structures. While the spatial envelopes of the forcing and response are similar, their internal phase and amplitude distributions across the different state variables are distinct. It is this structural difference that permits transient energy growth, confirming that the significant non-normality of the system is a highly localised phenomenon tied directly to the physics of the shock wave.

https://doi.org/10.1017/jfm.2026.11255 Published online by Cambridge University Press

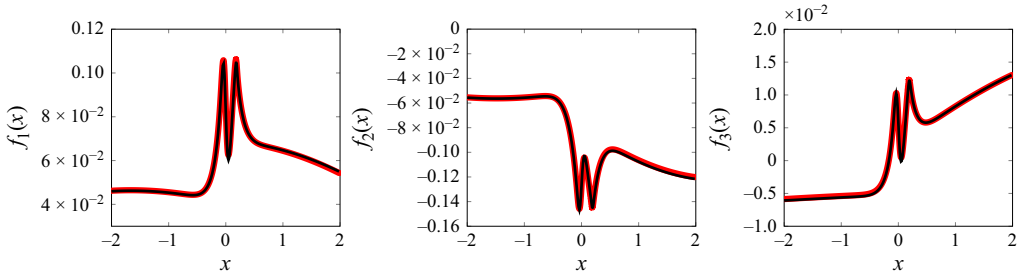


Figure 13. Numerical resolvent forcing mode solution (▬) and solution as per the viscous ($\mu = 5 \times 10^{-3}$) extension of Giles & Pierce (2001) (▬), corresponding to the transonic shock-laden flow through a quasi-1-D model of flow through a CD nozzle.

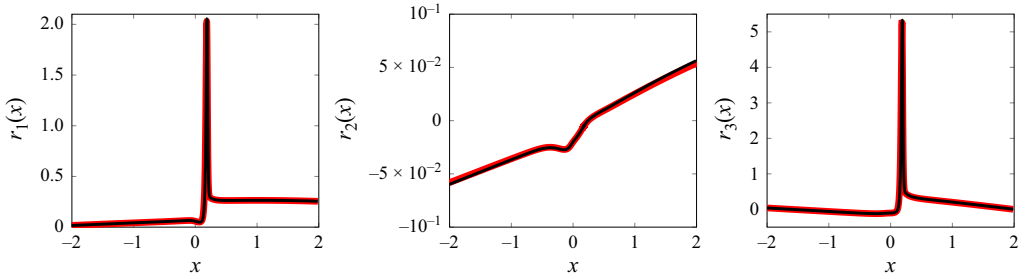


Figure 14. Numerical resolvent response mode solution (▬) and solution as per the viscous ($\mu = 5 \times 10^{-3}$) extension of Giles & Pierce (2001) (▬), corresponding to the transonic shock-laden flow through a quasi-1-D model of flow through a CD nozzle.

The steps involved in computing the semi-analytic resolvent mode solution, represented by the (4.28), are summarised as follows.

(i) The following two point boundary value problem is solved to compute the base-flow solution ($q(x)$ and thus $\boldsymbol{U}(x)$):

$$\frac{\mathrm{d}\left(\rho q^2 h + ph\right)}{\mathrm{d}x} - p\frac{\mathrm{d}h}{\mathrm{d}x} + \frac{4\mu}{3}\left(-\frac{\mathrm{d}\left(h\dfrac{\mathrm{d}q}{\mathrm{d}x}\right)}{\mathrm{d}x} + \frac{\mathrm{d}q}{\mathrm{d}x}\frac{\mathrm{d}h}{\mathrm{d}x}\right) = 0, \tag{4.29}$$

where $\rho = Q/(hq)$, $e = (H - (1/2)q^2)/\gamma$, $p = (\gamma - 1)\rho e$, with boundary conditions $q_{x,\mathrm{in}} = 0$, $q_{out} = \{(p_{out}^2 h_{out}^2 \gamma^2)/((\gamma - 1)^2 Q^2) + 2H\}^{1/2} - (\gamma p_{out} h_{out})/((\gamma - 1)Q)$.

(ii) Compute the homogeneous solutions $\hat{\boldsymbol{u}}_{i\in\{1,2,3\}}(x)$ as per (4.5) and the forcing vectors $\hat{\boldsymbol{f}}_{i\in\{1,2,3\}}(x)$ as per (4.24).

(iii) Select an initial guess for $\boldsymbol{f}_{n=1}$ and begin the power iteration method.

(a) To compute $\boldsymbol{r}_n(x) = \boldsymbol{G}_{viscous} * \boldsymbol{f}_n$, the response vector is assumed to have the following form (similar to the inviscid case)

$$\boldsymbol{r}_n(x) = \int_D \left\{\alpha_{n,1}(\xi)\,\boldsymbol{u}_1(x,\xi) + \alpha_{n,2}(\xi)\,\boldsymbol{u}_2(x,\xi) + \alpha_{n,3}(\xi)\,\boldsymbol{u}_3(x,\xi)\right\}\mathrm{d}\xi, \tag{4.30}$$

https://doi.org/10.1017/jfm.2026.11255 Published online by Cambridge University Press

such that

$$\boldsymbol{L}_{viscous}\left(x, \frac{\mathrm{d}}{\mathrm{d}x}, \frac{\mathrm{d}^2}{\mathrm{d}x^2}\right)\boldsymbol{r}_n(x) = \boldsymbol{f}_n(x). \tag{4.31}$$

Now, by applying the operator $\boldsymbol{L}_{viscous}$ to the integrand of (4.30), using a procedure similar to the derivation presented in Appendix G, (4.31) takes the following form:

$$\alpha_{n,i}(x)\hat{\boldsymbol{f}}_i(x) + \frac{\mathrm{d}\alpha_{n,i}(x)}{\mathrm{d}x}\left(h(x)\frac{\partial \boldsymbol{F}_{v,1}}{\partial \boldsymbol{U}}\hat{\boldsymbol{u}}_i(x)\right) = \boldsymbol{f}_n(x). \tag{4.32}$$

Solving this equation provides the $\alpha_{n,i}(x)$ terms, which are then substituted into (4.30) to obtain $\boldsymbol{r}_n(x)$.

(*b*) The forcing vector corresponding to the next iteration $\boldsymbol{f}_{n+1} = \boldsymbol{G}^{\dagger}_{viscous} * \boldsymbol{r}_n(x)$ is obtained by solving (4.17) with $\boldsymbol{r}_n(x)$ as the gradient $(\boldsymbol{g}_i(x))$ vector.

(iv) The sub-steps of step (iii) are repeated until $||\boldsymbol{G}^{\dagger}_{viscous} * \boldsymbol{G}_{viscous} * \boldsymbol{f}_n - \sigma^2\boldsymbol{f}_n||/||\sigma^2\boldsymbol{f}_n|| < 10^{-8}$.

Hence, figures 13 and 14 demonstrate that the viscous extension of the semi-analytic Green's function approach, which enables the semi-analytic resolvent analysis to account for both the system's responsiveness to external forcing and its receptivity to responses at the shock, can resolve the disagreement between the numerical and semi-analytic resolvent solutions. Therefore, when considering the resolvent response across a shock, it is crucial to consider numerical methods that specifically account for the receptivity across the shock to capture the leading resolvent modes about a shock-laden base flow.

The next section demonstrates how this semi-analytic approach for computing resolvent modes across shock-laden flows is able to choose an appropriately modified weighted essentially-non-oscillatory (WENO) scheme to compute their numerical resolvent modes accurately. Application to other numerical methods follows similarly.

5. Semi-analytic WENO modification for resolvent mode analysis of viscous shock-laden flows

The WENO (Jiang & Shu 1996; Martín *et al.* 2006; Nonomura *et al.* 2015; Li, Ju & Zhang 2017) family of schemes has proven effective for simulating shock-laden flows due to its robust nonlinear formulation.

The inviscid terms of the one-dimensional viscous Navier–Stokes equations are discretised with the characteristic-wise fifth-order finite-difference WENO-JS scheme of Jiang & Shu (1996) (see Appendix B for details). Numerical fluxes are obtained through a local Lax–Friedrichs splitting. Time advancement uses the classical fourth-order Runge–Kutta method. The physical viscous flux terms are discretised using a standard second-order central difference stencil. A smoothly stretched, non-uniform mesh is designed through a systematic grid-convergence study. Specifically, WENO dynamically adjusts the interpolation stencil weights in response to local smoothness indicators, enabling the method to maintain high accuracy in regions with smooth flow while ensuring stable shock-capturing capability. Notwithstanding these desirable properties, when WENO is employed to compute numerical resolvent modes as part of a linear or adjoint-based flow analysis, it can yield spurious mode structures at or near the shock discontinuity (it is important to note that the spurious mode structures can be further amplified according to the form of the quasi-1-D equations used in the numerical discretisation). These artefacts manifest as non-physical oscillations or distortions in the resolvent modes that do not

https://doi.org/10.1017/jfm.2026.11255 Published online by Cambridge University Press

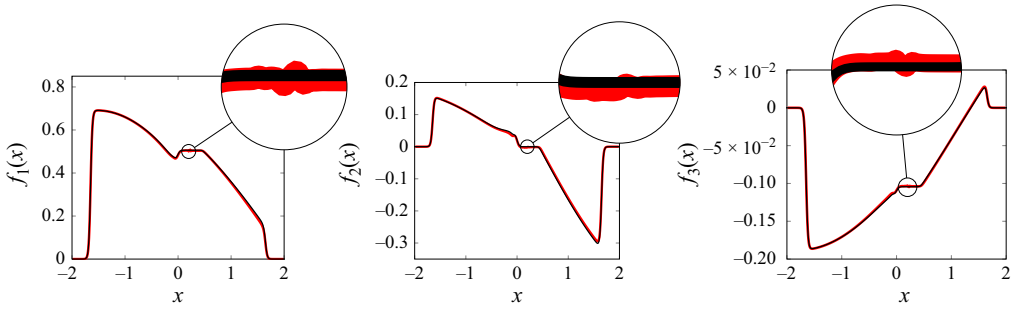


Figure 15. Numerical resolvent forcing mode solution using standard WENO (▬) and solution as per the viscous ($\mu = 5 \times 10^{-3}$) extension of Giles & Pierce (2001) (▬), corresponding to the transonic shock-laden flow through a quasi-1-D model of flow through a CD nozzle.

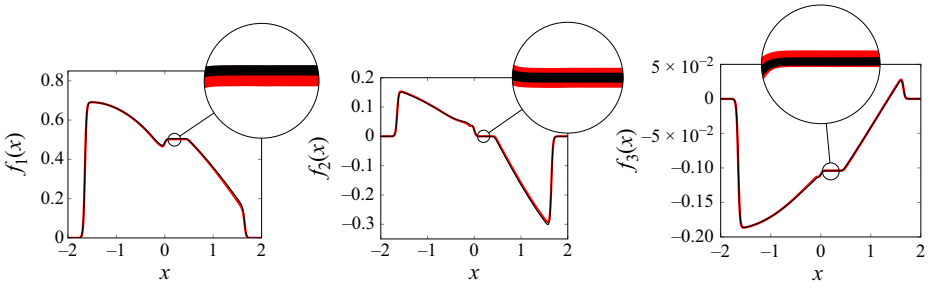


Figure 16. Numerical resolvent forcing mode solution using WENO with the smoothness indicators switched off (▬) and solution as per the viscous ($\mu = 5 \times 10^{-3}$) extension of Giles & Pierce (2001) (▬), corresponding to the transonic shock-laden flow through a quasi-1-D model of flow through a CD nozzle.

converge to the reference semi-analytic (viscous) solutions, as illustrated in figure 15. Using the same conditions as before, and using smoothed $\boldsymbol{B}$ and $\boldsymbol{C}$ operators,

$$\begin{aligned}\boldsymbol{C}(x) = &\left(\mathcal{H}_{smooth}\left(x - (x_s + \Delta x)\right) + \mathcal{H}_{smooth}\left(-(x - (x_s - \Delta x))\right)\right) \cdot \\ &\left(\mathcal{H}_{smooth}\left(x - (-x_d)\right) \cdot \mathcal{H}_{smooth}\left(-(x - x_d)\right)\right)\end{aligned} \tag{5.1}$$

and

$$\boldsymbol{B}(x) = \left(\mathcal{H}_{smooth}\left(x - (-x_d)\right)\right) \cdot \left(\mathcal{H}_{smooth}\left(-(x - x_d)\right)\right), \tag{5.2}$$

where $x_s = 0.18$, $x_d = 1.65$, $\Delta x = 0.25$ and $\mathcal{H}_{smooth} = 1/(1 + \exp(-60\,x))$. To reconcile the discrepancy between the WENO-based numerical modes and the semi-analytic reference, we propose a modified version of the WENO scheme in which the influence of the solution smoothness indicators – and hence, the nonlinear adaptation of the scheme – is disabled during resolvent mode calculations. This modification effectively linearises the WENO weighting procedure, mitigating the discontinuity-induced artefacts. Through this linearisation, the calculated resolvent forcing modes in shock-containing regions demonstrate improved agreement with the semi-analytic viscous solutions, as depicted in figures 16 and 17.

A similar strategy – disabling the nonlinear dissipation or adaptation terms to recover a consistent linear Jacobian – has been employed in the CFD literature, most prominently for the Jameson–Schmidt–Turkel (JST) scheme in the context of eigenvalue computations (Jameson, Schmidt & Turkel 1981), and likewise in time–stepping methods for linear stability analysis (Marquet, Sipp & Jacquin 2008). In contrast to JST's

https://doi.org/10.1017/jfm.2026.11255 Published online by Cambridge University Press

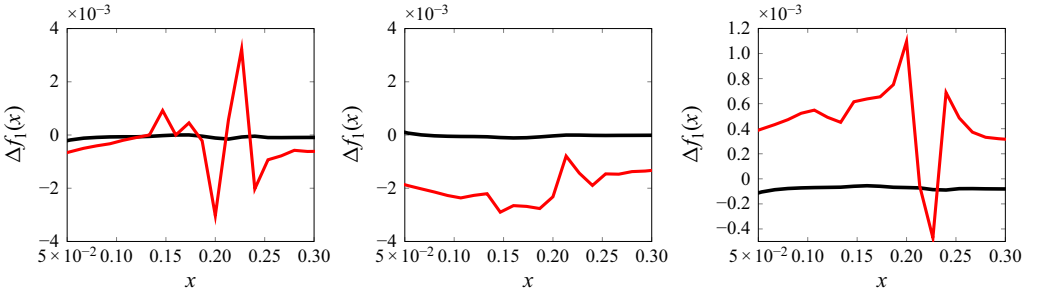


Figure 17. Difference between numerical resolvent forcing mode solutions using standard WENO (▬) and modified WENO (▬) schemes, compared with the viscous ($\mu = 5 \times 10^{-3}$) extension of Giles & Pierce (2001) for transonic shock-laden flow in a quasi-1-D CD nozzle model.

polynomial artificial dissipation, WENO's nonlinearity arises from the solution-dependent smoothness indicators and adaptive stencil weights, which imparts a more localised shock-capturing behaviour. Here, we demonstrate that these nonlinear weights – if left active – induce spurious oscillations in resolvent mode shapes across shock discontinuities and do not converge to the semi-analytic viscous reference. By turning off nonlinear modifications to the WENO weights during resolvent-mode computation, we recover a high-order accurate, shock-capturing finite-difference operator whose resolvent forcing and response modes align closely with the semi-analytic solutions. We emphasise that this modification is not intended as a replacement for the classical WENO formulation in general flow simulations, but rather as a precise tool for isolating the linear response in shock-laden resolvent analyses.

In doing so, the method preserves the desirable shock-capturing traits of WENO in simulating the shock-laden flows, while ensuring that the resolvent modes reflect more accurately the underlying physics predicted by semi-analytic solutions.

6. Conclusion

In this study, we developed semi-analytic resolvent solutions for shock-laden flows using the quasi-one-dimensional Euler and Navier–Stokes equations. By extending the Green's function approach to include both inviscid and viscous effects, we derived forward and adjoint Green's function operators that account for the presence of shocks. Our analysis revealed that shocks introduce heightened sensitivity in the resolvent operator to disturbances across flow discontinuities, which can lead to significant discrepancies between numerical and analytical solutions if not properly accounted for.

We demonstrated that incorporating viscosity into the resolvent analysis resolves these discrepancies by modelling the shock as a finite-thickness region with strong gradients. The semi-analytic solutions developed serve as valuable benchmarks for validating numerical schemes designed to compute adjoint and resolvent modes in shock-laden flows, ensuring they capture the correct physical behaviour.

These findings have important implications for flow control and stability analyses in high-speed aerodynamics, where shocks are prevalent. Accurate resolvent analyses that account for shocks are essential for designing effective control strategies and predicting flow instabilities.

The challenges identified for resolvent analysis – specifically, the heightened sensitivity to disturbances across shocks and the necessity of viscous regularisation – extend to other direct-adjoint methodologies. Linear stability analyses may exhibit spurious eigenvalues

https://doi.org/10.1017/jfm.2026.11255 Published online by Cambridge University Press

or non-convergence when shocks are treated as inviscid discontinuities, as the adjoint operator inherits singularities from the shock. Similarly, structural sensitivity maps (e.g. for identifying optimal control locations) could misrepresent the true sensitivity regions near shocks if viscous effects are neglected (Sartor, Mettot & Sipp 2015). Flow control strategies relying on adjoint-based gradients, such as shock-stabilisation or drag-reduction efforts, risk suboptimal or divergent solutions without regularisation mechanisms like viscosity or adjoint-consistent numerical schemes. Thus, the regularisation approaches validated here – both physical (viscosity) and numerical (modified discretisation) – are broadly relevant for robust adjoint frameworks in shock-laden flows.

Additionally, as part of our investigation into accurate resolvent analysis in shock-laden flows, we introduced a modification to the WENO scheme aimed at mitigating numerical artefacts near discontinuities. While the nonlinear nature of standard WENO schemes effectively captures shock waves and, in some cases, the choice of governing equation representation (quasi-1-D equations), its stencil adaptation based on solution smoothness can introduce spurious structures in the computed resolvent modes. By disabling the influence of these smoothness indicators, we retain the scheme's shock-capturing capability during the computation of the flow simulation, while eliminating un-physical oscillations in the results of the resolvent analysis. This modification shows excellent agreement with our semi-analytic, viscous-based resolvent solutions, thereby enhancing the predictive fidelity of numerical resolvent analyses in the presence of flow discontinuities.

Future work will focus on extending the current analysis to multidimensional flows and exploring the asymptotic behaviour of the viscous resolvent mode solutions as the viscosity parameter $\mu \to 0$. Additionally, investigating the application of these semi-analytic solutions to more complex geometries and flow conditions will further enhance our understanding of shock-induced phenomena in fluid mechanics.

Acknowledgements. We gratefully acknowledge the guidance and support of Dr. Steve Martens, the program officer for this project.

Funding. This research was supported by the Office of Naval Research (ONR) under grant number N00014-19-1-2431.

Declaration of interests. The authors report no conflict of interest.

Appendix A. Summary of the JST implementation

(i) *Domain and grid.* One-dimensional domain $x \in [-1, 1]$ with a uniform, cell-centred grid of $N = 401$ cells; $\Delta x = 2/N$. One ghost cell is used on each boundary.

(ii) *Nozzle geometry.*

$$h(x) = 2 - \exp(-x^2/\sigma^2), \quad \sigma = 0.3, \quad h_{j\pm(1/2)} = h\big((x_j + x_{j\pm1})/2\big). \tag{A1}$$

Gas model. Perfect gas with $\gamma = 1.4$.

(iii) *Time stepping.* Explicit classical RK4 with

$$\Delta t \;=\; 2^{-2}\,\frac{\mathrm{CFL}}{c_{max}\,\Delta x}, \tag{A2}$$

where c_{max} is estimated from the initial state.

(iv) *JST stabilisation.* Coefficients $k_2 = (1/2)$, $k_4 = (1/64)$, $c_{04} = 1$. The pressure sensor is

$$v_j = \left| \frac{p_{j+1} - 2p_j + p_{j-1}}{p_{j+1} + 2p_j + p_{j-1}} \right|, \tag{A3}$$

https://doi.org/10.1017/jfm.2026.11255 Published online by Cambridge University Press

and the second/fourth-order dissipation are $\varepsilon^{(2)}_{j+(1/2)} = k_2 \max(v_{j+1}, v_j)$, $\varepsilon^{(4)}_{j+(1/2)} = \max(0,\ k_4 - c_{04}\,\varepsilon^{(2)}_{j+(1/2)})$.

(v) *Boundary conditions.* Inflow: stagnation quantities $H_{in} = 4$, $P_{0,in} = 2$ (state reconstructed from an estimated M_{in}). Outflow: static pressure $P_{out} = 1.6$.

(vi) *Initial condition (uniform).*

$$\boldsymbol{U}(x, 0) = \begin{bmatrix} \rho \\ \rho u \\ \rho E \end{bmatrix} = \begin{bmatrix} 1.670728329772049 \\ 0.6405076279276232 \\ 4.808588314223788 \end{bmatrix}. \tag{A4}$$

Appendix B. Summary of the WENO implementation

We solve the quasi-1-D Euler equations for $\boldsymbol{U} = [\rho,\ \rho u,\ \rho E]^{\mathsf{T}}$ on a uniform grid x_j with spacing Δx. The nozzle area is $h(x) = 2 - \exp(-x^2/\sigma^2)$ with $\sigma = 0.3$; the geometric source is $(h'/h)\,[\rho u,\ \rho u^2,\ \rho u E + p u]^{\mathsf{T}}$. Perfect gas with $\gamma = 1.4$.

(i) *Convective fluxes.* Characteristic-wise fifth-order WENO reconstruction at faces $x_{j+1/2}$ using Roe-averaged eigenvectors. Lax–Friedrichs flux splitting with $\alpha = \max(|u - c|,\ |u|,\ |u + c|)$ over the local stencil; nonlinear weights with exponent $p \in \{2, 0\}$ and $\varepsilon = 10^{-6}$. The flux divergence is computed by the conservative difference

$$(\partial_x \boldsymbol{F})_j \approx \frac{\hat{\boldsymbol{f}}_{j+1/2} - \hat{\boldsymbol{f}}_{j-1/2}}{\Delta x}. \tag{B1}$$

Within three points of each boundary, a compatible sixth-order central surrogate is used.

(ii) *Regularisation.* A small artificial viscosity $\mu = 5 \times 10^{-3}$ is added via second derivatives of viscous-type fluxes using a symmetric 7-point stencil with coefficients $(\pm 2,\ \pm 27,\ \pm 270,\ -490)/180$, and a mixed term $(h'/h)\,\partial_x F_v^{(2)}$.

(iii) *Boundary conditions.* Three ghost cells per side. Inlet: $H_{in} = 4$, $P_{0,in} = 2$ with the local Mach estimated from interior states. Outlet: static pressure $P_{out} = 1.6$. Ghost states are filled by linear extrapolation consistent with these targets.

(iv) *Time integration.* Explicit classical RK4.

(v) *Constants.* $R = 1$, $c_p = \gamma R/(\gamma - 1)$, $Pr = 3/4$.

Appendix C. Summary of the viscous finite-volume implementation

We solve the quasi-1-D compressible Navier–Stokes equations in conservative form for $\boldsymbol{U} = [\rho,\ \rho u,\ \rho E]^{\mathsf{T}}$ with a perfect gas ($\gamma = 1.4$, $c_p = \gamma/(\gamma - 1)$, $Pr = 3/4$). The nozzle area is $h(x) = 2 - \exp(-x^2/\sigma^2)$ with $\sigma = 0.3$.

(i) *Mesh and unknowns.* Finite volumes on a smoothed non-uniform grid with cell centres x_j and faces $x_{j\pm(1/2)}$; one ghost cell per side. Cell size $\Delta x_j = x_{j+(1/2)} - x_{j-(1/2)}$.

(ii) *Semi-discrete update.* For each conserved component,

$$h_j \frac{d\boldsymbol{U}_j}{dt} = -\frac{(h\boldsymbol{F})_{j+\frac{1}{2}} - (h\boldsymbol{F})_{j-\frac{1}{2}}}{\Delta x_j} + \boldsymbol{S}_j, \qquad \boldsymbol{S}_j = \big[0,\ p_j h'(x_j),\ 0\big]^{\mathsf{T}}. \tag{C1}$$

https://doi.org/10.1017/jfm.2026.11255 Published online by Cambridge University Press

(iii) *Convective face flux.* Linear reconstruction on the non-uniform grid

$$\boldsymbol{F}_{j+(1/2)} = \boldsymbol{F}_j + \frac{\boldsymbol{F}_{j+1} - \boldsymbol{F}_j}{x_{j+1} - x_j}\left(x_{j+(1/2)} - x_j\right), \tag{C2}$$

without a Riemann solver.

(iv) *Viscous/regularisation terms.* Added at faces and differenced as

$$\begin{aligned} &\text{mass, } -\mu_{mod}\,\partial_x(\rho u); \quad \text{momentum, } -\frac{4}{3}\mu\partial_x u; \\ &\text{energy, } -\left[\frac{2}{3}\mu\partial_x(u^2) + c_p(\mu/Pr)\partial_x T\right]; \end{aligned} \tag{C3}$$

with face gradients from a local quadratic 3-point stencil on $\{j-1, j, j+1\}$ (exact non-uniform coefficients) and linearised geometric corrections proportional to $h'(x)\,u$. Typical coefficients in the code are: $\mu = 10^{-3}$ for time marching (no mass smoothing, $\mu_{mod} = 0$); $\mu = 5 \times 10^{-2}$ for the linearised/resolvent operator, $\mu_{mod} = 10^{-5}$.

(v) *Time integration.* Explicit classical RK4 with fixed Δt (e.g. 10^{-4}); marched to steady state by monitoring $\|\boldsymbol{U}^n - \boldsymbol{U}^{n-1}\|$.

(vi) *Boundary conditions.* Inlet at x_{min}: stagnation inputs $H_{in} = 4$, $P_{0,in} = 2$, with Mach estimated by linear extrapolation $M_{in} \approx (3/2)\,u_j/c_j - (1/2)\,u_{j+1}/c_{j+1}$, then $\boldsymbol{U}_{in}$ from isentropic relations. Outlet at x_{max}: impose static $P_{out} = 1.6$; ρ and u are linearly extrapolated before conversion to $\boldsymbol{U}_{out}$. End-face fluxes use $(hF)_{1/2} = h_{1/2}F(\boldsymbol{U}_{in})$ and $(hF)_{N+1/2} = h_{N+1/2}F(\boldsymbol{U}_{out})$.

(vii) *Analytical baseline.* Initial condition constructed from the area–Mach relation with a normal-shock closure to locate x_0, using the previous stagnation inputs.

(viii) *Linear operator and resolvent.* The Jacobian $\boldsymbol{L}$ is assembled by finite differences,

$$\boldsymbol{L}(:, i) \approx \frac{\mathrm{rhs}(\boldsymbol{U} + \varepsilon e_i) - \mathrm{rhs}(\boldsymbol{U})}{\varepsilon}, \qquad \varepsilon = 10^{-6}, \tag{C4}$$

then scaled by $\mathrm{diag}(h)$ and restricted to interior unknowns. The inner product uses $\boldsymbol{N} = \mathrm{diag}(\sqrt{\Delta x_{j\pm(1/2)}})$; the adjoint is $\boldsymbol{L}^* = (\boldsymbol{N}^\top\boldsymbol{N})^{-1}\boldsymbol{L}^\top(\boldsymbol{N}^\top\boldsymbol{N})$. Leading forcing/response modes are obtained by alternating solves with $\boldsymbol{L}^{-1}$ and $(\boldsymbol{L}^*)^{-1}$ (with zero padding where grids differ), followed by normalisation.

Appendix D. Further details of the resolvent analysis procedure

This section elaborates on the details of the resolvent analysis procedure described in § 2. We start with (2.6) and for the sake of clarity, define a new operator $\boldsymbol{A}$ as

$$\boldsymbol{A} = \boldsymbol{N}_r\boldsymbol{C}\boldsymbol{R}(\omega)\boldsymbol{B}\boldsymbol{N}_f^{-1} \tag{D1}$$

$$\Rightarrow \boldsymbol{A}\boldsymbol{A}^H\hat{\boldsymbol{w}} = \sigma^2\hat{\boldsymbol{y}}. \tag{D2}$$

Now, if we introduce a perturbation ($\boldsymbol{dL}$) to the linearised Navier–Stokes operator in (D1), we arrive at the following equation:

$$\begin{aligned} \left(\boldsymbol{N}_r\boldsymbol{C}(\boldsymbol{R} + \boldsymbol{dR})\boldsymbol{B}\boldsymbol{N}_f^{-1}\boldsymbol{N}_f^{-H}\boldsymbol{B}^H(\boldsymbol{R}^H + \boldsymbol{dR}^H)\boldsymbol{C}^H\boldsymbol{N}_r^H\right)(\hat{\boldsymbol{w}} + \boldsymbol{d}\hat{\boldsymbol{w}}) \\ = \left(\sigma^2 + 2\sigma d\sigma + \cdots\right)(\hat{\boldsymbol{w}} + \boldsymbol{d}\hat{\boldsymbol{w}}). \end{aligned} \tag{D3}$$

https://doi.org/10.1017/jfm.2026.11255 Published online by Cambridge University Press

We next expand the equation as

$$\begin{aligned}\left(\boldsymbol{A}+\boldsymbol{N}_r\boldsymbol{CdRBN}_f^{-1}\right)\left(\boldsymbol{A}^H+\boldsymbol{N}_f^{-H}\boldsymbol{B}^H\boldsymbol{dR}^H\boldsymbol{C}^H\boldsymbol{N}_r^H\right)(\hat{\boldsymbol{w}}+\boldsymbol{d}\hat{\boldsymbol{w}})\\ =\left(\sigma^2+2\sigma d\sigma+\cdots\right)(\hat{\boldsymbol{w}}+\boldsymbol{d}\hat{\boldsymbol{w}}),\end{aligned}\tag{D4}$$

observing that $\boldsymbol{AA}^H\hat{\boldsymbol{w}}=\sigma^2\hat{\boldsymbol{w}}$ and focusing on the first-order terms, we have

$$\begin{aligned}\Rightarrow \boldsymbol{AA}^H\boldsymbol{d}\hat{\boldsymbol{w}}+\left(\boldsymbol{N}_r\boldsymbol{CdRBN}_f^{-1}\boldsymbol{A}^H+\boldsymbol{AN}_f^{-H}\boldsymbol{B}^H\boldsymbol{dR}^H\boldsymbol{C}^H\boldsymbol{N}_r^H\right)\hat{\boldsymbol{w}}\\ =\sigma^2\boldsymbol{d}\hat{\boldsymbol{w}}+2\sigma\, d\sigma\,\hat{\boldsymbol{w}}.\end{aligned}\tag{D5}$$

Now, multiply the (D5) with $\hat{\boldsymbol{w}}^H$ and we get

$$\begin{aligned}\hat{\boldsymbol{w}}^H\boldsymbol{AA}^H\boldsymbol{d}\hat{\boldsymbol{w}}+\hat{\boldsymbol{w}}^H(\boldsymbol{N}_r\boldsymbol{CdRBN}_f^{-1}\boldsymbol{A}^H+\boldsymbol{AN}_f^{-H}\boldsymbol{B}^H\boldsymbol{dR}^H\boldsymbol{C}^H\boldsymbol{N}_r^H)\hat{\boldsymbol{w}}\\ =\sigma^2\hat{\boldsymbol{w}}^H\boldsymbol{d}\hat{\boldsymbol{w}}+2\sigma d\sigma\,\hat{\boldsymbol{w}}^H\hat{\boldsymbol{w}},\end{aligned}\tag{D6}$$

which can be further simplified by noting that $\hat{\boldsymbol{w}}^H\boldsymbol{AA}^H=\sigma^2\hat{\boldsymbol{w}}^H$, as

$$\Rightarrow \hat{\boldsymbol{w}}^H\left(\boldsymbol{N}_r\boldsymbol{CdRBN}_f^{-1}\boldsymbol{A}^H+\boldsymbol{AN}_f^{-H}\boldsymbol{B}^H\boldsymbol{dR}^H\boldsymbol{C}^H\boldsymbol{N}_r^H\right)\hat{\boldsymbol{w}}=2\sigma d\sigma\,\hat{\boldsymbol{w}}^H\hat{\boldsymbol{w}},\tag{D7}$$

$$\Rightarrow d\sigma=\frac{1}{2\sigma}\frac{\hat{\boldsymbol{w}}^H\left(\boldsymbol{N}_r\boldsymbol{CdRBN}_f^{-1}\boldsymbol{A}^H+\boldsymbol{AN}_f^{-H}\boldsymbol{B}^H\boldsymbol{dR}^H\boldsymbol{C}^H\boldsymbol{N}_r^H\right)\hat{\boldsymbol{w}}}{\hat{\boldsymbol{w}}^H\hat{\boldsymbol{w}}},\tag{D8}$$

however, $\boldsymbol{A}^H\hat{\boldsymbol{w}}=\sigma\hat{\boldsymbol{y}}$ (since $\boldsymbol{A}=\boldsymbol{WSY}^H$) and $\hat{\boldsymbol{w}}^H\boldsymbol{N}_r\boldsymbol{CdRBN}_f^{-1}\boldsymbol{A}^H\hat{\boldsymbol{w}}=(\hat{\boldsymbol{w}}\boldsymbol{AN}_f^{-H}\boldsymbol{B}^H\boldsymbol{dR}^H\boldsymbol{C}^H\boldsymbol{N}_r^H\hat{\boldsymbol{w}})^H$

$$\Rightarrow d\sigma=\mathrm{Re}\left(\hat{\boldsymbol{w}}^H\left(\boldsymbol{N}_r\boldsymbol{CdRBN}_f^{-1}\right)\hat{\boldsymbol{y}}/\left(\hat{\boldsymbol{w}}^H\hat{\boldsymbol{w}}\right)\right).\tag{D9}$$

Finally, as per (191) from Petersen & Pederson (2008),

$$(\boldsymbol{Q}+\alpha^2\boldsymbol{M})^{-1}\approx\boldsymbol{Q}^{-1}-\alpha^2\boldsymbol{Q}^{-1}\boldsymbol{M}\boldsymbol{Q}^{-1}.\tag{D10}$$

Here, $\boldsymbol{dR}$ can be expressed as a perturbation to the operator $\boldsymbol{L}$, represented by $\boldsymbol{dL}$, as

$$\left(\boldsymbol{R}^{-1}-\boldsymbol{dL}\right)^{-1}\approx\boldsymbol{R}+\boldsymbol{dR}\approx\boldsymbol{R}+\boldsymbol{RdLR}\tag{D11}$$

$$\Rightarrow \boldsymbol{dR}\approx\boldsymbol{RdLR}\tag{D12}$$

$$\Rightarrow d\sigma=\mathrm{Re}\left(\hat{\boldsymbol{w}}^H(\boldsymbol{N}_r\boldsymbol{C}(\boldsymbol{RdLR})\boldsymbol{BN}_f^{-1})\hat{\boldsymbol{y}}/(\hat{\boldsymbol{w}}^H\hat{\boldsymbol{w}})\right).\tag{D13}$$

https://doi.org/10.1017/jfm.2026.11255 Published online by Cambridge University Press

Appendix E. Integration by parts procedure to construct the viscous adjoint operator

The integration by parts procedure used to transfer the differential operator from $\boldsymbol{u}$ to the variable $\boldsymbol{v}$ is

$$\begin{aligned} I = & \int_D \boldsymbol{v}^T \cdot \boldsymbol{f}\, \mathrm{d}x \\ & - \int_D \boldsymbol{v}^T \cdot \left[\frac{\mathrm{d}}{\mathrm{d}x} \left(h \frac{\partial \boldsymbol{F}}{\partial \boldsymbol{U}}\, \boldsymbol{u} \right) \right] \mathrm{d}x \\ & - \int_D \boldsymbol{v}^T \cdot \left[\frac{\mathrm{d}}{\mathrm{d}x} \left(h \frac{\mathrm{d}}{\mathrm{d}x} \left(\frac{\partial \boldsymbol{F}_{v,1}}{\partial \boldsymbol{U}}\, \boldsymbol{u} \right) \right) \right] \mathrm{d}x \\ & - \int_D \boldsymbol{v}^T \cdot \left[\frac{\mathrm{d}h}{\mathrm{d}x} \frac{\mathrm{d}}{\mathrm{d}x} \left(\frac{\partial \boldsymbol{F}_{v,2}}{\partial \boldsymbol{U}}\, \boldsymbol{u} \right) \right] \mathrm{d}x \\ & + \int_D \boldsymbol{v}^T \cdot \frac{\mathrm{d}h}{\mathrm{d}x} \frac{\partial \boldsymbol{P}}{\partial \boldsymbol{U}}\, \boldsymbol{u}\, \mathrm{d}x \\ & + \int_D \left(\frac{\partial p}{\partial \boldsymbol{U}} \right)^T \cdot \boldsymbol{u}\, \mathrm{d}x, \end{aligned} \tag{E1}$$

$$\begin{aligned} I = & \int_D \boldsymbol{v}^T \cdot \boldsymbol{f}\, \mathrm{d}x \\ & - \left\{ \boldsymbol{v}^T \cdot \left(h \frac{\partial \boldsymbol{F}}{\partial \boldsymbol{U}}\, \boldsymbol{u} \right) \Big|_{x=x_{inlet}}^{x=x_{outlet}} - \int_D \left(h \frac{\partial \boldsymbol{F}}{\partial \boldsymbol{U}}\, \boldsymbol{u} \right)^T \cdot \frac{\mathrm{d}\boldsymbol{v}}{\mathrm{d}x}\, \mathrm{d}x \right\} \\ & - \left\{ \boldsymbol{v}^T \cdot \left(h \frac{\mathrm{d}}{\mathrm{d}x} \left(\frac{\partial \boldsymbol{F}_{v,1}}{\partial \boldsymbol{U}}\, \boldsymbol{u} \right) \right) \Big|_{x=x_{inlet}}^{x=x_{outlet}} - \int_D \left(h \frac{\mathrm{d}}{\mathrm{d}x} \left(\frac{\partial \boldsymbol{F}_{v,1}}{\partial \boldsymbol{U}}\, \boldsymbol{u} \right) \right)^T \cdot \frac{\mathrm{d}\boldsymbol{v}}{\mathrm{d}x}\, \mathrm{d}x \right\} \\ & - \left\{ \left(\frac{\mathrm{d}h}{\mathrm{d}x} \boldsymbol{v} \right)^T \cdot \left(\frac{\partial \boldsymbol{F}_{v,2}}{\partial \boldsymbol{U}}\, \boldsymbol{u} \right) \Big|_{x=x_{inlet}}^{x=x_{outlet}} - \int_D \left(\frac{\partial \boldsymbol{F}_{v,2}}{\partial \boldsymbol{U}}\, \boldsymbol{u} \right)^T \cdot \frac{\mathrm{d}}{\mathrm{d}x} \left(\frac{\mathrm{d}h}{\mathrm{d}x} \boldsymbol{v} \right) \mathrm{d}x \right\} \\ & + \int_D \boldsymbol{u}^T \frac{\mathrm{d}h}{\mathrm{d}x} \frac{\partial \boldsymbol{P}}{\partial \boldsymbol{U}}^T \boldsymbol{v}\, \mathrm{d}x \\ & + \int_D \left(\frac{\partial p}{\partial \boldsymbol{U}} \right)^T \cdot \boldsymbol{u}\, \mathrm{d}x, \end{aligned} \tag{E2}$$

substituting $\boldsymbol{A} = (\partial \boldsymbol{F}/\partial \boldsymbol{U})$, $\boldsymbol{C}_1 = (\partial \boldsymbol{F}_{v,1}/\partial \boldsymbol{U})$, $\boldsymbol{C}_2 = (\partial \boldsymbol{F}_{v,2}/\partial \boldsymbol{U})$, $\boldsymbol{B} = (\partial \boldsymbol{P}/\partial \boldsymbol{U})$ and $\boldsymbol{g} = (\partial p/\partial \boldsymbol{U})$, we have

$$\begin{aligned} I = & \int_D \boldsymbol{v}^T \cdot \boldsymbol{f}\, \mathrm{d}x \\ & - \left\{ \boldsymbol{v}^T \cdot (h \boldsymbol{A} \boldsymbol{u}) \Big|_{x=x_{inlet}}^{x=x_{outlet}} - \int_D \boldsymbol{u}^T \cdot \left(h \boldsymbol{A}^T \frac{\mathrm{d}\boldsymbol{v}}{\mathrm{d}x} \right) \mathrm{d}x \right\} \\ & - \left\{ \boldsymbol{v}^T \cdot \left(h \frac{\mathrm{d}}{\mathrm{d}x} (\boldsymbol{C}_1 \boldsymbol{u}) \right) \Big|_{x=x_{inlet}}^{x=x_{outlet}} - \int_D h \frac{\mathrm{d}v^T}{\mathrm{d}x} \cdot \left(\frac{\mathrm{d}}{\mathrm{d}x} (\boldsymbol{C}_1 \boldsymbol{u}) \right) \mathrm{d}x \right\} \end{aligned}$$

https://doi.org/10.1017/jfm.2026.11255 Published online by Cambridge University Press

$$
\begin{aligned}
&- \left\{ \left(\frac{\mathrm{d}h}{\mathrm{d}x} \boldsymbol{v} \right)^T \cdot (\boldsymbol{C}_2 \boldsymbol{u}) \Big|_{x=x_{inlet}}^{x=x_{outlet}} - \int_D \boldsymbol{u}^T \cdot \left(\boldsymbol{C}_2^T \frac{\mathrm{d}}{\mathrm{d}x} \left(\frac{\mathrm{d}h}{\mathrm{d}x} \boldsymbol{v} \right) \right) \mathrm{d}x \right\} \mathrm{d}x \\
&+ \int_D \boldsymbol{u}^T \cdot \left(\frac{\mathrm{d}h}{\mathrm{d}x} \boldsymbol{B}^T \boldsymbol{v} \right) \mathrm{d}x \\
&+ \int_D \boldsymbol{g}^T \cdot \boldsymbol{u} \, \mathrm{d}x, \qquad \text{(E3)}
\end{aligned}
$$

$$
\begin{aligned}
I = &\int_D \boldsymbol{v}^T \cdot \boldsymbol{f} \, \mathrm{d}x \\
&- \left\{ \boldsymbol{v}^T \cdot (h \boldsymbol{A} \boldsymbol{u}) \Big|_{x=x_{inlet}}^{x=x_{outlet}} - \int_D \boldsymbol{u}^T \cdot \left(h \boldsymbol{A}^T \frac{\mathrm{d}\boldsymbol{v}}{\mathrm{d}x} \right) \mathrm{d}x \right\} \\
&- \left\{ \boldsymbol{v}^T \cdot \left(h \frac{\mathrm{d}}{\mathrm{d}x} (\boldsymbol{C}_1 \boldsymbol{u}) \right) \Big|_{x=x_{inlet}}^{x=x_{outlet}} \right. \\
&\left. - \left[\frac{\mathrm{d}\boldsymbol{v}^T}{\mathrm{d}x} \cdot (h \boldsymbol{C}_1 \boldsymbol{u}) \Big|_{x=x_{inlet}}^{x=x_{outlet}} - \int_D \boldsymbol{u}^T \cdot \left(\boldsymbol{C}_1^T \frac{\mathrm{d}}{\mathrm{d}x} \left(h \frac{\mathrm{d}\boldsymbol{v}}{\mathrm{d}x} \right) \right) \mathrm{d}x \right] \right\} \\
&- \left\{ \left(\frac{\mathrm{d}h}{\mathrm{d}x} \boldsymbol{v} \right)^T \cdot (\boldsymbol{C}_2 \boldsymbol{u}) \Big|_{x=x_{inlet}}^{x=x_{outlet}} - \int_D \boldsymbol{u}^T \cdot \left(\boldsymbol{C}_2^T \frac{\mathrm{d}}{\mathrm{d}x} \left(\frac{\mathrm{d}h}{\mathrm{d}x} \boldsymbol{v} \right) \right) \mathrm{d}x \right\} \mathrm{d}x \\
&+ \int_D \boldsymbol{u}^T \cdot \left(\frac{\mathrm{d}h}{\mathrm{d}x} \boldsymbol{B}^T \boldsymbol{v} \right) \mathrm{d}x \\
&+ \int_D \boldsymbol{g}^T \cdot \boldsymbol{u} \, \mathrm{d}x, \qquad \text{(E4)}
\end{aligned}
$$

$$
\begin{aligned}
I = &\int_D \boldsymbol{v}^T \cdot \boldsymbol{f} \, \mathrm{d}x \\
&- \left[\boldsymbol{v}^T \cdot (h \boldsymbol{A} \boldsymbol{u}) \right]_{x=x_{inlet}}^{x=x_{outlet}} - \left[\boldsymbol{v}^T \cdot \left(h \frac{\mathrm{d}}{\mathrm{d}x} (\boldsymbol{C}_1 \boldsymbol{u}) \right) \right]_{x=x_{inlet}}^{x=x_{outlet}} + \left[\frac{\mathrm{d}\boldsymbol{v}^T}{\mathrm{d}x} \cdot (h \boldsymbol{C}_1 \boldsymbol{u}) \right]_{x=x_{inlet}}^{x=x_{outlet}} \\
&- \left[\left(\frac{\mathrm{d}h}{\mathrm{d}x} \boldsymbol{v} \right)^T \cdot (\boldsymbol{C}_2 \boldsymbol{u}) \right]_{x=x_{inlet}}^{x=x_{outlet}} \\
&- \int_D \boldsymbol{u}^T \cdot \left(-h \boldsymbol{A}^T \frac{\mathrm{d}\boldsymbol{v}}{\mathrm{d}x} + \boldsymbol{C}_1^T \frac{\mathrm{d}}{\mathrm{d}x} \left(h \frac{\mathrm{d}\boldsymbol{v}}{\mathrm{d}x} \right) - \boldsymbol{C}_2^T \frac{\mathrm{d}}{\mathrm{d}x} \left(\frac{\mathrm{d}h}{\mathrm{d}x} \boldsymbol{v} \right) - \frac{\mathrm{d}h}{\mathrm{d}x} \boldsymbol{B}^T \boldsymbol{v} - \boldsymbol{g} \right) \mathrm{d}x, \qquad \text{(E5)}
\end{aligned}
$$

$$
\begin{aligned}
I = &\int_D \boldsymbol{v}^T \cdot \boldsymbol{f} \, \mathrm{d}x \\
&- \left[\boldsymbol{v}^T \cdot (h \boldsymbol{A} \boldsymbol{u}) \right]_{x=x_{inlet}}^{x=x_{outlet}} - \left[\boldsymbol{v}^T \cdot \left(h \frac{\mathrm{d}}{\mathrm{d}x} (\boldsymbol{C}_1 \boldsymbol{u}) \right) \right]_{x=x_{inlet}}^{x=x_{outlet}} + \left[\frac{\mathrm{d}\boldsymbol{v}^T}{\mathrm{d}x} \cdot (h \boldsymbol{C}_1 \boldsymbol{u}) \right]_{x=x_{inlet}}^{x=x_{outlet}} \\
&- \left[\left(\frac{\mathrm{d}h}{\mathrm{d}x} \boldsymbol{v} \right)^T \cdot (\boldsymbol{C}_2 \boldsymbol{u}) \right]_{x=x_{inlet}}^{x=x_{outlet}} \\
&- \int_D \boldsymbol{u}^T \cdot \left(\boldsymbol{L}^\dagger \boldsymbol{v} - \boldsymbol{g} \right) \mathrm{d}x. \qquad \text{(E6)}
\end{aligned}
$$

https://doi.org/10.1017/jfm.2026.11255 Published online by Cambridge University Press

Appendix F. Derivation of the objective function perturbation when impulse forcing is applied

Equation (4.12) can be transformed to a form similar to (4.8) as shown in the following, using an integration by parts procedure and preserving the terms $\boldsymbol{u}(x,\xi)$ or $\boldsymbol{f}(\xi)\delta(x-\xi)$ throughout this procedure,

$$\begin{aligned} I(\xi) = &\int_D \boldsymbol{v}^T(x)\cdot\boldsymbol{f}(\xi)\delta(x-\xi)\,\mathrm{d}x \\ &-\left[\boldsymbol{v}^T(x)\cdot(h\boldsymbol{A}\boldsymbol{u}(x,\xi))\right]_{x=x_{inlet}}^{x=x_{outlet}} - \left[\boldsymbol{v}^T(x)\cdot\left(h\frac{\mathrm{d}}{\mathrm{d}x}\left(\boldsymbol{C}_1\boldsymbol{u}(x,\xi)\right)\right)\right]_{x=x_{inlet}}^{x=x_{outlet}} \\ &+\left[\frac{\mathrm{d}\boldsymbol{v}^T(x)}{\mathrm{d}x}\cdot\left(h\boldsymbol{C}_1\boldsymbol{u}(x,\xi)\right)\right]_{x=x_{inlet}}^{x=x_{outlet}} - \left[\left(\frac{\mathrm{d}h}{\mathrm{d}x}\boldsymbol{v}(x)\right)^T\cdot\left(\boldsymbol{C}_2\boldsymbol{u}(x,\xi)\right)\right]_{x=x_{inlet}}^{x=x_{outlet}} \\ &-\int_D \boldsymbol{u}^T(x,\xi)\cdot\left(\boldsymbol{L}^\dagger\boldsymbol{v}-\boldsymbol{g}\right)\mathrm{d}x. \end{aligned} \tag{F1}$$

Assuming $\boldsymbol{L}^\dagger\boldsymbol{v}-\boldsymbol{g}=\boldsymbol{0}$ and using (4.11), we have

$$\begin{aligned} I(\xi) = &\int_D \boldsymbol{v}^T(x)\cdot\{\boldsymbol{L}_{viscous}\boldsymbol{u}(x,\xi)\}\;\mathrm{d}x - \left[\boldsymbol{v}^T(x)\cdot(h\boldsymbol{A}\boldsymbol{u}(x,\xi))\right]_{x=x_{inlet}}^{x=x_{outlet}} \\ &-\left[\boldsymbol{v}^T(x)\cdot\left(h\frac{\mathrm{d}}{\mathrm{d}x}\left(\boldsymbol{C}_1\boldsymbol{u}(x,\xi)\right)\right)\right]_{x=x_{inlet}}^{x=x_{outlet}} + \left[\frac{\mathrm{d}\boldsymbol{v}^T(x)}{\mathrm{d}x}\cdot\left(h\boldsymbol{C}_1\boldsymbol{u}(x,\xi)\right)\right]_{x=x_{inlet}}^{x=x_{outlet}} \\ &-\left[\left(\frac{\mathrm{d}h}{\mathrm{d}x}\boldsymbol{v}(x)\right)^T\cdot\left(\boldsymbol{C}_2\boldsymbol{u}(x,\xi)\right)\right]_{x=x_{inlet}}^{x=x_{outlet}} \end{aligned} \tag{F2}$$

$$\begin{aligned} = &\left\{\boldsymbol{v}^T(x)\cdot\left(h(x)\boldsymbol{A}\hat{\boldsymbol{p}}_1(x)\right) + \boldsymbol{v}^T(x)\cdot\left(h(x)\frac{\mathrm{d}}{\mathrm{d}x}\left(\boldsymbol{C}_1\hat{\boldsymbol{p}}_1(x)\right)\right)\right. \\ &\left.+\,\boldsymbol{v}^T(x)\cdot\left(\frac{\mathrm{d}h(x)}{\mathrm{d}x}\boldsymbol{C}_2\hat{\boldsymbol{p}}_1(x)\right) - \frac{\mathrm{d}\boldsymbol{v}^T(x)}{\mathrm{d}x}\cdot\left(h(x)\boldsymbol{C}_1\hat{\boldsymbol{p}}_1(x)\right)\right\}\Big|_{x=\xi} \\ &+\left[\boldsymbol{v}^T(x)\cdot\left(h(x)\boldsymbol{C}_1\hat{\boldsymbol{p}}(x)\right)\delta(x-\xi)\right]_{x=x_{inlet}}^{x=x_{outlet}} \\ &-\left[\boldsymbol{v}^T(x)\cdot(h\boldsymbol{A}\boldsymbol{u}(x,\xi))\right]_{x=x_{inlet}}^{x=x_{outlet}} - \left[\boldsymbol{v}^T(x)\cdot\left(h\frac{\mathrm{d}}{\mathrm{d}x}\left(\boldsymbol{C}_1\boldsymbol{u}(x,\xi)\right)\right)\right]_{x=x_{inlet}}^{x=x_{outlet}} \\ &-\left[\boldsymbol{v}^T(x)\cdot\left(\frac{\mathrm{d}h}{\mathrm{d}x}\boldsymbol{C}_2\boldsymbol{u}(x,\xi)\right)\right]_{x=x_{inlet}}^{x=x_{outlet}} + \left[\frac{\mathrm{d}\boldsymbol{v}^T(x)}{\mathrm{d}x}\cdot\left(h\boldsymbol{C}_1\boldsymbol{u}(x,\xi)\right)\right]_{x=x_{inlet}}^{x=x_{outlet}}, \end{aligned} \tag{F3}$$

where the solution $\boldsymbol{u}(x,\xi)$ is assumed to have the form $H(x-\xi)\hat{\boldsymbol{p}}_1(x)+\hat{\boldsymbol{p}}_2(x)$ and both $\hat{\boldsymbol{p}}_{i=1,2}$ are homogeneous solutions that satisfy $\boldsymbol{L}_{viscous}\hat{\boldsymbol{p}}_i=\boldsymbol{0}$.

https://doi.org/10.1017/jfm.2026.11255 Published online by Cambridge University Press

Appendix G. The derivation of the viscous forward forcing functions

In this appendix, the forcing vector for the forward problem is derived as

$$
\begin{aligned}
\hat{\boldsymbol{f}}_i(x) &= \int_D \delta(x-\xi)\ \hat{\boldsymbol{f}}_i(\xi)\,\mathrm{d}\xi \\
&= \int_D \boldsymbol{L}_{viscous}\tilde{\boldsymbol{u}}_i(x,\xi)\,\mathrm{d}\xi \\
&= \int_D \left\{ \frac{\mathrm{d}}{\mathrm{d}x}\left(h\frac{\partial \boldsymbol{F}}{\partial \boldsymbol{U}}\tilde{\boldsymbol{u}}_i(x,\xi)\right) + \frac{\mathrm{d}}{\mathrm{d}x}\left(h\frac{\mathrm{d}}{\mathrm{d}x}\left(\frac{\partial \boldsymbol{F}_{v,1}}{\partial \boldsymbol{U}}\tilde{\boldsymbol{u}}_i(x,\xi)\right)\right) + \frac{\mathrm{d}h}{\mathrm{d}x}\frac{\mathrm{d}}{\mathrm{d}x}\left(\frac{\partial \boldsymbol{F}_{v,2}}{\partial \boldsymbol{U}}\ \tilde{\boldsymbol{u}}_i(x,\xi)\right) \right. \\
&\quad \left. -\frac{\mathrm{d}h}{\mathrm{d}x}\frac{\partial \boldsymbol{P}}{\partial \boldsymbol{U}}\tilde{\boldsymbol{u}}_i(x,\xi)\right\}\mathrm{d}\xi \\
&= \int_D \left\{ \mathscr{H}(x-\xi)\ \frac{\mathrm{d}}{\mathrm{d}x}\left(h(x)\ \frac{\partial \boldsymbol{F}}{\partial \boldsymbol{U}}\hat{\boldsymbol{u}}_i(x)\right) + \frac{\mathrm{d}\mathscr{H}(x-\xi)}{\mathrm{d}x}\left(h(x)\ \frac{\partial \boldsymbol{F}}{\partial \boldsymbol{U}}\hat{\boldsymbol{u}}_i(x)\right) \right. \\
&\quad + \frac{\mathrm{d}}{\mathrm{d}x}\left[h(x)\ \mathscr{H}(x-\xi)\ \frac{\mathrm{d}}{\mathrm{d}x}\left(\frac{\partial \boldsymbol{F}_{v,1}}{\partial \boldsymbol{U}}\hat{\boldsymbol{u}}_i(x)\right) + h(x)\ \frac{\mathrm{d}\mathscr{H}(x-\xi)}{\mathrm{d}x}\ \left(\frac{\partial \boldsymbol{F}_{v,1}}{\partial \boldsymbol{U}}\hat{\boldsymbol{u}}_i(x)\right)\right] \\
&\quad + \mathscr{H}(x-\xi)\ \frac{\mathrm{d}h}{\mathrm{d}x}\frac{\mathrm{d}}{\mathrm{d}x}\left(\frac{\partial \boldsymbol{F}_{v,2}}{\partial \boldsymbol{U}}\ \hat{\boldsymbol{u}}_i(x)\right) + \ \frac{\mathrm{d}\mathscr{H}(x-\xi)}{\mathrm{d}x}\ \left(\frac{\mathrm{d}h}{\mathrm{d}x}\frac{\partial \boldsymbol{F}_{v,2}}{\partial \boldsymbol{U}}\ \hat{\boldsymbol{u}}_i(x)\right) \\
&\quad \left. - \mathscr{H}(x-\xi)\ \frac{\mathrm{d}h(x)}{\mathrm{d}x}\ \frac{\partial \boldsymbol{P}}{\partial \boldsymbol{U}}\hat{\boldsymbol{u}}_i(x)\right\}\mathrm{d}\xi \\
&= \int_D \left\{ \mathscr{H}(x-\xi)\ \cancelto{0}{\boldsymbol{L}_{viscous}\hat{\boldsymbol{u}}_i(x)} + \frac{\mathrm{d}\mathscr{H}(x-\xi)}{\mathrm{d}x}\left(h(x)\ \frac{\partial \boldsymbol{F}}{\partial \boldsymbol{U}}\hat{\boldsymbol{u}}_i(x)\right) \right. \\
&\quad + \frac{\mathrm{d}\mathscr{H}(x-\xi)}{\mathrm{d}x}\ h(x)\ \frac{\mathrm{d}}{\mathrm{d}x}\left(\frac{\partial \boldsymbol{F}_{v,1}}{\partial \boldsymbol{U}}\hat{\boldsymbol{u}}_i(x)\right) + \frac{\mathrm{d}}{\mathrm{d}x}\left[h(x)\ \frac{\mathrm{d}\mathscr{H}(x-\xi)}{\mathrm{d}x}\left(\frac{\partial \boldsymbol{F}_{v,1}}{\partial \boldsymbol{U}}\hat{\boldsymbol{u}}_i(x)\right)\right] \\
&\quad \left. + \frac{\mathrm{d}\mathscr{H}(x-\xi)}{\mathrm{d}x}\ \left(\frac{\mathrm{d}h}{\mathrm{d}x}\frac{\partial \boldsymbol{F}_{v,2}}{\partial \boldsymbol{U}}\ \hat{\boldsymbol{u}}_i(x)\right)\right\}\mathrm{d}\xi \\
&= \int_D \left\{ \frac{\mathrm{d}\mathscr{H}(x-\xi)}{\mathrm{d}x}\left(h(x)\ \frac{\partial \boldsymbol{F}}{\partial \boldsymbol{U}}\hat{\boldsymbol{u}}_i(x)\right) + \frac{\mathrm{d}\mathscr{H}(x-\xi)}{\mathrm{d}x}\ h(x)\ \frac{\mathrm{d}}{\mathrm{d}x}\left(\frac{\partial \boldsymbol{F}_{v,1}}{\partial \boldsymbol{U}}\hat{\boldsymbol{u}}_i(x)\right) \right. \\
&\quad + \frac{\mathrm{d}}{\mathrm{d}x}\left[h(x)\ \frac{\mathrm{d}\mathscr{H}(x-\xi)}{\mathrm{d}x}\left(\frac{\partial \boldsymbol{F}_{v,1}}{\partial \boldsymbol{U}}\hat{\boldsymbol{u}}_i(x)\right)\right] + \ \frac{\mathrm{d}\mathscr{H}(x-\xi)}{\mathrm{d}x}\ \left(\frac{\mathrm{d}h}{\mathrm{d}x}\frac{\partial \boldsymbol{F}_{v,2}}{\partial \boldsymbol{U}}\ \hat{\boldsymbol{u}}_i(x)\right) \left. \right\}\mathrm{d}\xi \\
&= \int_D \left\{ \delta(x-\xi)\left(h(x)\ \frac{\partial \boldsymbol{F}}{\partial \boldsymbol{U}}\hat{\boldsymbol{u}}_i(x)\right) + \delta(x-\xi)\ h(x)\ \frac{\mathrm{d}}{\mathrm{d}x}\left(\frac{\partial \boldsymbol{F}_{v,1}}{\partial \boldsymbol{U}}\hat{\boldsymbol{u}}_i(x)\right) \right. \\
&\quad + \frac{\mathrm{d}}{\mathrm{d}x}\left[h(x)\ \delta(x-\xi)\left(\frac{\partial \boldsymbol{F}_{v,1}}{\partial \boldsymbol{U}}\hat{\boldsymbol{u}}_i(x)\right)\right] + \ \delta(x-\xi)\left(\frac{\mathrm{d}h}{\mathrm{d}x}\frac{\partial \boldsymbol{F}_{v,2}}{\partial \boldsymbol{U}}\ \hat{\boldsymbol{u}}_i(x)\right) \left. \right\}\mathrm{d}\xi \\
&= h(x)\ \frac{\partial \boldsymbol{F}}{\partial \boldsymbol{U}}\hat{\boldsymbol{u}}_i(x) + h(x)\ \frac{\mathrm{d}}{\mathrm{d}x}\left(\frac{\partial \boldsymbol{F}_{v,1}}{\partial \boldsymbol{U}}\hat{\boldsymbol{u}}_i(x)\right) + \frac{\mathrm{d}h}{\mathrm{d}x}\left(\frac{\partial \boldsymbol{F}_{v,2}}{\partial \boldsymbol{U}}\hat{\boldsymbol{u}}_i(x)\right) \\
&\quad + \frac{\mathrm{d}}{\mathrm{d}x}\left[h(x)\ \cancelto{1}{\int_D \delta(x-\xi)\mathrm{d}\xi}\left(\frac{\partial \boldsymbol{F}_{v,1}}{\partial \boldsymbol{U}}\hat{\boldsymbol{u}}_i(x)\right)\right] \\
\Rightarrow \hat{\boldsymbol{f}}_i(x) &= h(x)\ \frac{\partial \boldsymbol{F}}{\partial \boldsymbol{U}}\hat{\boldsymbol{u}}_i(x) \ + \ h(x)\ \frac{\mathrm{d}}{\mathrm{d}x}\left(\frac{\partial \boldsymbol{F}_{v,1}}{\partial \boldsymbol{U}}\hat{\boldsymbol{u}}_i(x)\right) \\
&\quad + \frac{\mathrm{d}}{\mathrm{d}x}\left[h(x)\ \left(\frac{\partial \boldsymbol{F}_{v,1}}{\partial \boldsymbol{U}}\hat{\boldsymbol{u}}_i(x)\right)\right] + \ \frac{\mathrm{d}h}{\mathrm{d}x}\left(\frac{\partial \boldsymbol{F}_{v,2}}{\partial \boldsymbol{U}}\hat{\boldsymbol{u}}_i(x)\right). \qquad \text{(G1)}
\end{aligned}
$$

https://doi.org/10.1017/jfm.2026.11255 Published online by Cambridge University Press

Appendix H. The derivation of the viscous adjoint solutions

In this appendix, details of the steps taken to solve (4.17) are presented. Similar to § 3.3, the approach is to setup three equations to compute the three components of the viscous adjoint solution $\boldsymbol{v}_i$ corresponding to a gradient function $\boldsymbol{g}_i$. The three equations correspond to three instances of (4.17) instantiated by the following three choices of linearly independent forward solutions:

$$\boldsymbol{u}_1(x,\xi) = \mathscr{H}(x-\xi)\left(\frac{1}{h(x)}\frac{\partial \boldsymbol{U}}{\partial m}\bigg|_{H,q} + c_m(x)\,\frac{\partial \boldsymbol{U}}{\partial q}\bigg|_{m,H}\right), \tag{H1}$$

$$\boldsymbol{u}_2(x,\xi) = \mathscr{H}(x-\xi)\left(\frac{\partial \boldsymbol{U}}{\partial H}\bigg|_{m,q} + c_H(x)\,\frac{\partial \boldsymbol{U}}{\partial q}\bigg|_{m,H}\right), \tag{H2}$$

$$\boldsymbol{u}_3(x,\xi) = \mathscr{H}(-(x-\xi))\left(\frac{1}{h(x)}\frac{\partial \boldsymbol{U}}{\partial m}\bigg|_{H,q} + c_q(x)\,\frac{\partial \boldsymbol{U}}{\partial q}\bigg|_{m,H}\right). \tag{H3}$$

Substituting these values for $\boldsymbol{u}_i(x,\xi)$ into (4.17) gives the following three linearly independent scalar equations:

$$\begin{aligned}
&v_{i,1}(\xi,\eta)\\
&= \mathscr{H}(\eta-\xi)\begin{bmatrix} -\dfrac{(mhc_m(\eta)-q(\eta))}{h(\eta)q(\eta)^2} \\ \dfrac{1}{h(\eta)} \\ \dfrac{c_m(\eta)\left((\gamma-1)mhq(\eta)^2-2Hmh\right)+2Hq(\eta)+(\gamma-1)q(\eta)^3}{2\gamma h(\eta)q(\eta)^2}\end{bmatrix}\cdot \boldsymbol{g}_i(\eta)\\
&\quad + \frac{1}{6\gamma q(\xi)^2}\begin{pmatrix} 8\gamma\mu h(\xi)\,q(\xi)^2\,c_m(\xi)' - 8\gamma\mu c_m(\xi)\,q(\xi)^2\,h'(\xi)\\ +6\gamma H\,mhc_m(\xi) - 6H\,mhc_m(\xi)\\ -3\gamma\,mhc_m(\xi)\,q(\xi)^2 - 3\,mhc_m(\xi)\,q(\xi)^2\\ -6\gamma H\,q(\xi) + 6H\,q(\xi)\\ -3\gamma\,q(\xi)^3 - 3q(\xi)^3\end{pmatrix} v_{i,2}(\xi,\eta)\\
&\quad - \frac{4}{3}\mu c_m(\xi)\,h(\xi)\,\frac{\partial v_{i,2}(\xi,\eta)}{\partial \xi}\\
&\quad - H v_{i,3}(\xi,\eta),
\end{aligned} \tag{H4}$$

$$\mathscr{H}(\eta-\xi)\begin{bmatrix} -\dfrac{mhc_H(\eta)}{h(\eta)q(\eta)^2} \\ 0 \\ \dfrac{mhc_H(\eta)\left((\gamma-1)q(\eta)^2-2H\right)+2q(\eta)}{2\gamma h(\eta)q(\eta)^2}\end{bmatrix}\cdot \boldsymbol{g}_i(\eta)$$

https://doi.org/10.1017/jfm.2026.11255 Published online by Cambridge University Press

$$+\begin{pmatrix} -c_H'(\xi)+\dfrac{c_H(\xi)h'(\xi)}{h(\xi)} \\ +\dfrac{3Hmhc_H(\xi)}{4\gamma\mu h(\xi)q(\xi)^2}-\dfrac{3Hmhc_H(\xi)}{4\mu h(\xi)q(\xi)^2} \\ +\dfrac{3mhc_H(\xi)}{8\gamma\mu h(\xi)}+\dfrac{3mhc_H(\xi)}{8\mu h(\xi)} \\ -\dfrac{3mh}{4\gamma\mu h(\xi)q(\xi)}+\dfrac{3mh}{4\mu h(\xi)q(\xi)} \end{pmatrix} v_{i,2}(\xi,\eta)$$
$$+c_H(\xi)\,\frac{\partial v_{i,2}(\xi,\eta)}{\partial\xi}$$
$$+\frac{3mh}{4\mu h(\xi)}\,v_{i,3}(\xi,\eta)$$
$$+\frac{\partial v_{i,3}(\xi,\eta)}{\partial\xi}=0, \tag{H5}$$

$$\frac{3\,\mathscr{H}(\eta-\xi)}{4\mu c_q(\xi)h(\xi)}\begin{bmatrix} -\dfrac{mhc_q(\eta)}{h(\eta)q(\eta)^2} \\ 0 \\ \dfrac{c_q(\eta)\left((\gamma-1)\,mhq(\eta)^2-2Hmh\right)}{2\gamma h(\eta)q(\eta)^2} \end{bmatrix}\cdot\boldsymbol{g}_i(\eta)$$
$$+\begin{pmatrix} \dfrac{3mh}{8\gamma\mu h(\xi)}+\dfrac{3mh}{8\mu h(\xi)} \\ +\dfrac{3Hmh}{4\gamma\mu h(\xi)q(\xi)^2}-\dfrac{3Hmh}{4\mu h(\xi)q(\xi)^2} \\ +\dfrac{h'(\xi)}{h(\xi)}-\dfrac{c_q'(\xi)}{c_q(\xi)} \end{pmatrix} v_{i,2}(\xi,\eta)$$
$$+\frac{\partial v_{i,2}(\xi,\eta)}{\partial\xi}=0, \tag{H6}$$

with the following boundary conditions:

$$\left.\frac{\partial^2 v_{i,2}(\xi,\eta)}{\partial\xi^2}\right|_{\xi=2}=0, \tag{H7}$$

$$\left.\frac{\partial^2 v_{i,3}(\xi,\eta)}{\partial\xi^2}\right|_{\xi=-2}=0. \tag{H8}$$

Appendix I. Derivation of the inviscid adjoint solution $\boldsymbol{v}(\boldsymbol{x})$ for a given $\boldsymbol{g}(\boldsymbol{\eta})$

To make explicit how (3.18) together with the linearised objective functional (3.14), the adjoint representation (3.16) and the adjoint Green's function definition (3.17) combine to obtain an expression for $\boldsymbol{v}(x)$, the following detailed derivation is presented.

First, we collect the three adjoint solutions in the matrix

$$\boldsymbol{V}(x,\eta):=\left(\boldsymbol{v}_1(x,\eta)\;\middle|\;\boldsymbol{v}_2(x,\eta)\;\middle|\;\boldsymbol{v}_3(x,\eta)\right), \tag{I1}$$

https://doi.org/10.1017/jfm.2026.11255 Published online by Cambridge University Press

and the quantities $I_{i,j}$ in the 3×3 matrix

$$\boldsymbol{I}(x,\eta) := \left[I_{i,j}(x,\eta)\right]_{i,j=1}^{3}. \tag{I2}$$

From (3.16), we can write

$$\boldsymbol{V}(x,\eta) = \boldsymbol{W}^{-T}(x)\boldsymbol{I}^{T}(x,\eta), \tag{I3}$$

where we have introduced

$$\boldsymbol{W}(x) := \left(\boldsymbol{f}_1(x) \mid \boldsymbol{f}_2(x) \mid \boldsymbol{f}_3(x)\right). \tag{I4}$$

Next, we express (3.14) in matrix form. Define

$$\boldsymbol{T}(\eta) := \left(\boldsymbol{g}_1(\eta) \mid \boldsymbol{g}_2(\eta) \mid \boldsymbol{g}_3(\eta)\right), \tag{I5}$$

$$\boldsymbol{U}(\eta,x) := \left(\boldsymbol{u}_1(\eta,x) \mid \boldsymbol{u}_2(\eta,x) \mid \boldsymbol{u}_3(\eta,x)\right), \tag{I6}$$

$$\boldsymbol{k}(\eta) := \begin{bmatrix} k_1(\eta) \\ k_2(\eta) \\ k_3(\eta) \end{bmatrix} = \begin{bmatrix} p(\eta) \\ T(\eta) \\ q(\eta) \end{bmatrix}, \tag{I7}$$

$$\boldsymbol{\delta}(x) := \begin{bmatrix} \delta_1(x) \\ \delta_2(x) \\ \delta_3(x) \end{bmatrix}, \tag{I8}$$

so that the first term in (3.14) can be written as

$$I_{i,j}^{(1)}(x,\eta) = \boldsymbol{u}_j(\eta,x)\cdot\boldsymbol{g}_i(\eta) \quad\Longrightarrow\quad \boldsymbol{I}^{(1)}(x,\eta) = \boldsymbol{T}^{T}(\eta)\,\boldsymbol{U}(\eta,x). \tag{I9}$$

The shock-related terms in (3.14) give

$$I_{i,j}^{(s)}(x,\eta) = \left[-\delta(\eta-x_s^{+}) + \delta(\eta-x_s^{-})\right] k_i(\eta)\,\delta_j(x), \tag{I10}$$

so that, in matrix form,

$$\boldsymbol{I}^{(s)}(x,\eta) = \boldsymbol{k}(\eta)\left[-\delta(\eta-x_s^{+}) + \delta(\eta-x_s^{-})\right]\boldsymbol{\delta}^{T}(x). \tag{I11}$$

Combining these expressions and transposing, we obtain

$$\boldsymbol{I}^{T}(x,\eta) = \boldsymbol{U}^{H}(\eta,x)\,\boldsymbol{T}(\eta) + \boldsymbol{\delta}(x)\left[-\delta(\eta-x_s^{+}) + \delta(\eta-x_s^{-})\right]\boldsymbol{k}^{T}(\eta), \tag{I12}$$

where $(\cdot)^{H}$ denotes the Hermitian transpose (which coincides with the transpose for real-valued variables).

Substituting (I12) into (I3) yields

$$\boldsymbol{V}(x,\eta) = \boldsymbol{W}^{-T}(x)\,\boldsymbol{U}^{H}(\eta,x)\,\boldsymbol{T}(\eta) + \boldsymbol{W}^{-T}(x)\,\boldsymbol{\delta}(x)\left[-\delta(\eta-x_s^{+}) + \delta(\eta-x_s^{-})\right]\boldsymbol{k}^{T}(\eta). \tag{I13}$$

Using the definition (3.17) of the adjoint Green's function,

$$\boldsymbol{G}^{\dagger}(x,\eta) = \boldsymbol{V}(x,\eta)\,\boldsymbol{T}^{-1}(\eta), \tag{I14}$$

we obtain

$$\begin{aligned}\boldsymbol{G}^{\dagger}(x,\eta) &= \boldsymbol{W}^{-T}(x)\boldsymbol{U}^{H}(\eta,x)\,\underbrace{\boldsymbol{T}(\eta)\boldsymbol{T}^{-1}(\eta)}_{=\boldsymbol{I}} \\ &\quad + \boldsymbol{W}^{-T}(x)\boldsymbol{\delta}(x)\left[-\delta(\eta-x_s^{+}) + \delta(\eta-x_s^{-})\right]\boldsymbol{k}^{T}(\eta)\,\boldsymbol{T}^{-1}(\eta) \\ &= \boldsymbol{W}^{-T}(x)\boldsymbol{U}^{H}(\eta,x) \\ &\quad + \boldsymbol{W}^{-T}(x)\boldsymbol{\delta}(x)\left[-\delta(\eta-x_s^{+}) + \delta(\eta-x_s^{-})\right]\boldsymbol{k}^{T}(\eta)\,\boldsymbol{T}^{-1}(\eta).\end{aligned} \tag{I15}$$

https://doi.org/10.1017/jfm.2026.11255 Published online by Cambridge University Press

Finally, inserting this expression into (3.18) gives

$$\begin{aligned}\boldsymbol{v}(x) &= \int_D \boldsymbol{G}^{\dagger}(x,\eta)\boldsymbol{g}(\eta)\,\mathrm{d}\eta \\ &= \int_D \boldsymbol{W}^{-T}(x)\boldsymbol{U}^{H}(\eta,x)\boldsymbol{g}(\eta)\mathrm{d}\eta \\ &\quad + \boldsymbol{W}^{-T}(x)\boldsymbol{\delta}(x)\int_D \left[-\delta(\eta-x_s^{+})+\delta(\eta-x_s^{-})\right]\left[\boldsymbol{k}^{T}(\eta)\boldsymbol{T}^{-1}(\eta)\boldsymbol{g}(\eta)\right]\mathrm{d}\eta. \end{aligned} \tag{I16}$$

Using the properties of the Dirac delta,

$$\int_D \delta(\eta-x_s^{\pm})\,F(\eta)\,\mathrm{d}\eta = F(x_s^{\pm}), \tag{I17}$$

we obtain

$$\int_D \left[-\delta(\eta-x_s^{+})+\delta(\eta-x_s^{-})\right]F(\eta)\,\mathrm{d}\eta = -\left[F(\eta)\right]_{x_s^-}^{x_s^+}, \tag{I18}$$

so that, with $F(\eta)=\boldsymbol{k}^{T}(\eta)\boldsymbol{T}^{-1}(\eta)\boldsymbol{g}(\eta)$,

$$\boldsymbol{v}(x) = \int_D \boldsymbol{W}^{-T}(x)\boldsymbol{U}^{H}(\eta,x)\boldsymbol{g}(\eta)\,\mathrm{d}\eta - \boldsymbol{W}^{-T}(x)\boldsymbol{\delta}(x)\left[\boldsymbol{k}^{T}(\eta)\boldsymbol{T}^{-1}(\eta)\boldsymbol{g}(\eta)\right]_{x_s^-}^{x_s^+}. \tag{I19}$$

For the present choice of basis, only the first and third perturbations move the shock, so that $\delta_2(x)=0$ and

$$\boldsymbol{\delta}(x) = \begin{Bmatrix}\delta_1(x)\\ 0\\ \delta_3(x)\end{Bmatrix}, \quad \boldsymbol{k}^{T}(\eta) = \big(p(\eta)T(\eta)q(\eta)\big). \tag{I20}$$

Thus, we arrive at

$$v(x) = \int_D \boldsymbol{W}^{-T}(x)\begin{bmatrix}u_1(\eta,x)^H\\ u_2(\eta,x)^H\\ u_3(\eta,x)^H\end{bmatrix} g(\eta)\,\mathrm{d}\eta - \boldsymbol{W}^{-T}(x)\begin{Bmatrix}\delta_1(x)\\ 0\\ \delta_3(x)\end{Bmatrix}\left[(pTq)\boldsymbol{T}^{-1}(\eta)\boldsymbol{g}(\eta)\right]_{x_s^-}^{x_s^+}, \tag{I21}$$

where

$$\boldsymbol{W}(x) = \left(\boldsymbol{f}_1(x)\;\middle|\;\boldsymbol{f}_2(x)\;\middle|\;\boldsymbol{f}_3(x)\right), \qquad \boldsymbol{T}(\eta) = \left(\boldsymbol{g}_1(\eta)\;\middle|\;\boldsymbol{g}_2(\eta)\;\middle|\;\boldsymbol{g}_3(\eta)\right). \tag{I22}$$

References

Bagheri, S., Åkervik, E., Brandt, L. & Henningson, D.S. 2009 Matrix-free methods for the stability and control of boundary layers. *AIAA J.* **47** (5), 1057–1068.

Bodony, D.J. & Fikl, A. 2022 Adjoint-based sensitivity of shock-laden flows. In *Proceedings of the 2022 Summer Program, Center for Turbulence Research*, pp. 401–408. Center for Turbulence Research (CTR), Stanford University.

D'yakov, S.P. 1954 Shock wave stability. *Zh. Eksp. Teor. Fiz.* **27** (3), 288–295.

Fedorov, A. 2011 Transition and stability of high-speed boundary layers. *Annu. Rev. Fluid Mech.* **43** (1), 79–95.

Giles, M., Pierce, N., Giles, M. & Pierce, N. 1997 Adjoint equations in cfd-duality, boundary conditions and solution behaviour. In *13th Computational Fluid Dynamics Conference*, p. 1850. American Institute of Aeronautics and Astronautics (AIAA).

Giles, M.B. & Pierce, N.A. 2000 An introduction to the adjoint approach to design. *Flow Turbul. Combust.* **65**, 393–415.

https://doi.org/10.1017/jfm.2026.11255 Published online by Cambridge University Press

GILES, M.B. & PIERCE, N.A. 2001 Analytic adjoint solutions for the quasi-one-dimensional Euler equations. *J. Fluid Mech.* **426**, 327–345.
GUDERLEY, K.G. 1942 Starke kugelige und zylindrische verdichtungsstosse in der nahe des kugelmitterpunktes bnw. der zylinderachse. *Luftfahrtforschung* **19**, 302.
HALKO, N., MARTINSSON, P.-G. & TROPP, J.A. 2011 Finding structure with randomness: probabilistic algorithms for constructing approximate matrix decompositions. *SIAM Rev.* **53** (2), 217–288.
HERRMANN, B., BADDOO, P.J., SEMAAN, R., BRUNTON, S.L. & MCKEON, B.J. 2021 Data-driven resolvent analysis. *J. Fluid Mech.* **915**, A5.
JAMESON, A. 2017 Origins and further development of the Jameson–Schmidt–Turkel scheme. *AIAA J.* **55** (5), 1487–1510.
JAMESON, A., SCHMIDT, W. & TURKEL, E. 1981 Numerical solution of the euler equations by finite volume methods using Runge Kutta time stepping schemes. In *I4th Fluid and Plasma Dynamics Conference*, p. 1259. American Institute of Aeronautics and Astronautics (AIAA).
JIANG, G.-S. & SHU, C.-W. 1996 Efficient implementation of weighted eno schemes. *J. Comput. Phys.* **126** (1), 202–228.
LI, J., LUO, J., LIU, F., ZHENG, Y. & HAN, Z. 2024 Performance sensitivity analysis and aerodynamic optimization of compressor cascades by a turbulence adjoint method. *AIP Adv.* **14** (11), 115307.
LI, Z., JU, Y. & ZHANG, C. 2017 Hybrid central–weno scheme for the large eddy simulation of turbulent flows with shocks. *Numer. Heat Transfer, Part B: Fundam.* **72** (2), 170–189.
LIBERTY, E., WOOLFE, F., MARTINSSON, P.-G., ROKHLIN, V. & TYGERT, M. 2007 Randomized algorithms for the low-rank approximation of matrices. *Proc. Acad. Nat. Sci.* **104** (51), 20167–20172.
LOISEAU, J.-C., BUCCI, M.A., CHERUBINI, S. & ROBINET, J.-C. 2019 Time-stepping algorithms for large-scale resolvent analysis. *J. Comput. Phys.* **376**, 272–297.
LOZANO, C. 2016 A note on the dual consistency of the discrete adjoint quasi-one-dimensional Euler equations with cell-centered and cell-vertex central discretizations. *Comput. Fluids* **134**, 51–60.
LOZANO, C. & PONSIN, J. 2012 Remarks on the numerical solution of the adjoint quasi-one-dimensional Euler equations. *Intl J. Numer. Meth. Fluids* **69** (5), 966–982.
MACK, L.M. 1984 Special course on stability and transition of laminar flow. *AGARD Report*, 709.
MARQUET, O., SIPP, D. & JACQUIN, L. 2008 Sensitivity analysis and passive control of cylinder flow. *J. Fluid Mech.* **615**, 221–252.
MARTÍN, M.P., TAYLOR, E.M., WU, M. & WEIRS, V.G. 2006 A bandwidth-optimized weno scheme for the effective direct numerical simulation of compressible turbulence. *J. Comput. Phys.* **220** (1), 270–289.
MARTINI, E., RODRÍGUEZ, D., TOWNE, A. & CAVALIERI, A.V.G. 2020 Resolvent-based optimal estimation of turbulent channel flow. *J. Fluid Mech.* **900**, A2.
MCKEON, B.J. & SHARMA, A.S. 2010 A critical-layer framework for turbulent pipe flow. *J. Fluid Mech.* **658**, 336–382.
MOARREF, R., SHARMA, A.S., TROPP, J.A. & MCKEON, B.J. 2013 Model-based scaling of the streamwise energy density in high-Reynolds-number turbulent channels. *J. Fluid Mech.* **734**, 275–316.
MONOKROUSOS, A., KERVIK, E., BRANDT, L. & HENNINGSON, D.S. 2010 Global three-dimensional optimal disturbances in the blasius boundary-layer flow using time-steppers. *J. Fluid Mech.* **650**, 181–214.
MURTHY, S.R. & BODONY, D.J. 2024 Reducing jet noise from a biconical nozzle. In *30th AIAA/CEAS Aeroacoustics Conference (2024)*. Available at: https://arc.aiaa.org/doi/abs/10.2514/6.2024-3306.
NONOMURA, T., TERAKADO, D., ABE, Y. & FUJII, K. 2015 A new technique for freestream preservation of finite-difference WENO on curvilinear grid. *Comput. Fluids* **107**, 242–255.
PETERSEN, K.B. & PEDERSEN, M.S. 2008 The matrix cookbook. *Tech. Univ. Denmark* **7** (15), 510.
QADRI, U.A. & SCHMID, P.J. 2017 Frequency selection mechanisms in the flow of a laminar boundary layer over a shallow cavity. *Phys. Rev. Fluids* **2** (1), 013902.
REUTHER, J., ALONSO, J.J., RIMLINGER, M.J. & JAMESON, A. 1999 Aerodynamic shape optimization of supersonic aircraft configurations via an adjoint formulation on distributed memory parallel computers. *Comput. Fluids* **28** (4–5), 675–700.
SARTOR, F., METTOT, C. & SIPP, D. 2015 Stability, receptivity, and sensitivity analyses of buffeting transonic flow over a profile. *AIAA J.* **53** (7), 1980–1993.
SCHMID, P.J. 2007 Nonmodal stability theory. *Annu. Rev. Fluid Mech.* **39**, 129–162.

https://doi.org/10.1017/jfm.2026.11255 Published online by Cambridge University Press